Bone remodelling analysis of the humerus after resurfacing and stemless shoulder arthroplasties

Beatriz Ferreira dos Santos

Thesis to obtain the Master of Science Degree in

Biomedical Engineering

Supervisors: Professor João Orlando Marques Gameiro Folgado
Professor Carlos Miguel Fernandes Quental

Examination Committee

Chairperson: Professor Fernando Manuel Fernandes Simões
Supervisor: Professor Carlos Miguel Fernandes Quental
Members of the committee: Professor Paulo Rui Alves Fernandes
Doctor Marco Aurelio Carmelino Cardoso Sarmento

November 2017

Abstract

Although the shoulder arthroplasty has undergone evident advances over the last years, several complications still limit its success. New implant designs, such as resurfacing and stemless implants, have been developed to improve the long-term outcomes of shoulder arthroplasty and to provide an improved bone quality in revision operations. However, it is well known from Wolff's law that the introduction of an implant into the bone changes its natural load distribution, leading to a significant reduction in bone mass, which can compromise the long-term stability of the implant. The aim of the present study is to analyse the bone remodelling process of the humerus after resurfacing and stemless shoulder arthroplasties using three-dimensional finite element models.

The 3D geometric model of the humerus was generated from the Visible Human Project data. The resurfacing and stemless implants were modelled in Solidworks. The bone remodelling model applied is based on a global optimization criterion that considers both structural stiffness and the metabolic cost of bone maintenance. The loading condition considered comprised 6 load cases related to different positions of abduction in the frontal plane and anterior flexion in the sagittal plane. The forces applied, which included muscle forces and the reaction force at the shoulder joint, were estimated by a multibody model of the upper limb. The bone remodelling simulations were performed considering a healthy condition and a poor bone quality condition. The results were analysed qualitatively and quantitatively by comparing the bone density distribution obtained for the humerus without an implant to that obtained for the implanted humerus.

The results showed similar levels of bone resorption for the resurfacing and stemless implants. Nevertheless, the stemless implant lost less density at the implant fixation, which suggests that the stemless implants may be better supported in the long-term, and thus could lead to a better outcome than the resurfacing implants. For the poor bone quality condition, the loss of bone increased, which supports the limited performance of these implants for reduced bone stock.

Keywords: Shoulder joint, shoulder arthroplasty, stemless implant, resurfacing implant, bone remodeling, finite element method.

Resumo

Embora a artroplastia do ombro tenha sofrido avanços significativos nos últimos anos, várias complicações limitam ainda o seu sucesso. Novos implantes, tais como implantes de superfície e sem haste, têm sido desenvolvidos para melhorar os resultados a longo prazo da artroplastia do ombro, bem como para fornecer uma melhor qualidade óssea em cirurgias de revisão. No entanto, pela lei de Wolff sabe-se que a introdução de um implante no osso altera a sua distribuição natural de carga, levando a uma redução significativa da massa óssea, o que pode comprometer a estabilidade do implante a longo prazo. O objectivo do presente estudo é analisar o processo de remodelação óssea do úmero após artroplastias de superfície e sem haste do ombro, usando modelos de elementos finitos tridimensionais.

O modelo geométrico 3D do úmero foi gerado a partir dos dados do Visible Human Project. Os implantes de superfície e sem haste foram modelados em Solidworks. O modelo de remodelação óssea utilizado baseia-se num critério de optimização global que considera tanto a rigidez estrutural, como o custo metabólico para a manutenção de osso. O carregamento considerado é composto por 6 casos de carga, relativos a diferentes posições de abdução no plano frontal e flexão anterior no plano sagital. As forças aplicadas, que incluem as forças musculares e a força de reacção na articulação do ombro, foram estimadas a partir de um modelo de corpos múltiplos do membro superior. As simulações de remodelação óssea foram realizadas considerando uma condição saudável e uma condição de osso com baixa qualidade. Os resultados foram analisados qualitativamente e quantitativamente, comparando a distribuição de densidade óssea obtida para o úmero sem implante, com a obtida para o úmero implantado.

Os resultados demonstraram níveis de reabsorção óssea semelhantes para o implante de superfície e para o implante sem haste. No entanto, para o implante sem haste, verificou-se uma menor diminuição de densidade na região de fixação deste, o que sugere que os implantes sem haste podem fornecer um melhor suporte a longo prazo, podendo assim conduzir a um melhor resultado relativamente aos implantes de superfície. No caso de osso com baixa qualidade, a perda óssea aumentou, o que reforça a ideia de que o desempenho deste tipo de implantes é pior quando a qualidade do osso é menor.

Palavras-chave: articulação do ombro, artroplastia do ombro, implante sem haste, implante de superfície, remodelação óssea, método de elementos finitos.

Acknowledgments

I would first like to thank my supervisors, Professor João Folgado and Professor Carlos Quental, for their invaluable guidance and solicitude during the development of this work. This accomplishment would not have been possible without their useful comments and support throughout the learning process over the last few months.

I would also like to express my gratitude to Doctor Jacinto Monteiro and Doctor Marco Sarmento for their readiness to answer my questions regarding the medical issues.

To my parents and my sister, I cannot but offer my sincere thanks for always being around when I needed you most.

Finally, I express my deepest gratitude to my friends for all the inspiration and happiness that they bring to my life.

The work was funded by Fundação para a Ciência e Tecnologia through IDMEC, under LAETA, project UID/EMS/50022/2013.

Table of contents

List of figures

List of tables

List of acronyms

3D	Three-dimensional
TSA	Total shoulder arthroplasty
RTSA	Reverse total shoulder arthroplasty
FE	Finite element
FEM	Finite element method
CT	Computed tomography
VHP	Visible Human Project
HU	Hounsfield units
ROI	Region of interest
RMS	Root-mean-square
SD	Standard deviation

List of symbols

$\boldsymbol{a}, a_i$	Microstructure parameters
$\boldsymbol{\theta}, \theta_{\mathrm{i}}$	Euler angles
ρ	Relative density
ρ_{ap}	Apparent density
E^H_{ijkm}	Homogenized material properties tensor
E_{ijkl}	Material properties of the base material
Y	Domain of the unit cell
Y	Solid part of the unit cell domain
χ^{kl}	Set of periodic functions from the homogenization method
Ω	Volume of a body
Γ	Boundary surface of a body
$\boldsymbol{t}$	Surface loads
$\boldsymbol{u}$	Displacements field
$\boldsymbol{v}$	Virtual displacements field
α^P	Weight factor of load P
ε	Strain field
k	Metabolic cost per unit of bone volume
m	Corrective factor for the preservation of intermediate densities
s	Step length of the optimization problem
$\boldsymbol{D}$	Descent direction
ζ	Stabilization parameter of the optimization problem
H	Height
R	Radius
D	Diameter
μ	Attenuation value
ν	Poisson's coefficient
E	Young's modulus

Chapter 1

Introduction

1.1 Motivation and objectives

The shoulder joint replacement by an implant, commonly referred as shoulder arthroplasty, is an effective treatment for several shoulder pathologies and has demonstrated positive clinical outcomes over the years. However, it is associated with a set of complications that may compromise its long term performance. Of particular concern regarding the humeral component are component loosening and periprosthetic fracture complications (Bohsali et al., 2017). Although the reason behind these complications is not yet fully understood, studies on the hip and shoulder suggest that the implant's stability can be affected by stress shielding. This phenomenon is characterized by an adaptation of bone as a result of changes in the distribution of load due to the insertion of the implant (Nagels et al., 2003; Quental et al., 2012).

Bearing in mind that shoulder arthroplasty has become an option not only for a population with a higher average life expectancy, but also for younger and more active patients, new implants have been developed to improve the long term outcomes of shoulder arthroplasty and to provide ease of revision with improved bone quality, if needed. In order to reduce humeral stem complications, progressive shortening of the stem along with cementless application techniques have been developed (Churchill & Athwal, 2016). Over the last few years, resurfacing humeral implants have gained popularity by allowing the preservation of the majority of the humeral head, with minimal bone resection; however, with difficult exposure for glenoid replacement (Burgess et al., 2009; Churchill & Athwal, 2016; Schmidutz et al., 2014). Short- and medium-term studies demonstrate positive functional results, but it is known from the hip that resurfacing implants also affect the distribution of natural bone loading, inducing stress shielding (Gupta et al., 2006; Ong et al., 2006; Schmidutz et al., 2014). Stemless humeral implants emerged with the aim of completely avoiding stem-related complications while maintaining an optimal bone quality in revision surgeries and providing an optimal access for glenoid replacement (Churchill & Athwal, 2016). Although there is still reduced information available regarding a comprehensive assessment of stemless implants, Razfar et al. (2015) compared the proximal humeral stresses between three different stem length implants; they found that reducing the stem length may decrease stress shielding of the proximal bone, leading to a better mimicking of the intact bone.

In the literature, few studies address resurfacing and stemless shoulder arthroplasties, and only recently has the phenomenon of stress shielding been evaluated by assessing the difference in bone deformation before and after a shoulder arthroplasty with two different resurfacing implants (Schmidutz et al., 2014). Although the existence of stress shielding has been demonstrated, the bone adaptation process was not effectively modelled. Moreover, a single load condition was considered without the action of muscle forces, which certainly affected the characterization of the mechanical environment of the bone.

The purpose of this study is to investigate the process of bone remodelling of the humerus in the presence of resurfacing and stemless implants using three-dimensional finite element models. Six load cases, related to different positions of abduction in the frontal plane and flexion in the sagittal plane are considered, including muscle forces and the reaction force at the shoulder joint. Furthermore, a poorer bone condition is also considered to investigate the effect of bone quality on the adaptation process.

1.2 Thesis Structure

The present work is structured into six main chapters. The first chapter, in which this section is included, constitutes an introductory chapter that includes the motivation and objectives of this dissertation.

In Chapter 2, a brief introduction of the concepts involved in the context of this work is presented. First of all, some key anatomical concepts are provided. Then, a fundamental overview of the anatomical and physiological features of the shoulder complex is presented. At last, the existing shoulder arthroplasty prostheses and component options are detailed, along with a literature review on the background of biomechanical modelling.

Chapter 3 describes the fundamental concepts of the bone remodelling model used in this work.

In chapter 4, a detailed description of the computational work and methodology adopted in this dissertation is provided. It includes the steps followed to create the geometric models of the humerus and implants; the description of the finite element models and the validation of the bone remodelling model for intact bone; the decisions taken for the bone remodelling model after the shoulder arthroplasty; and finally, the method used to analyse the results.

Chapter 5 presents the results of the bone remodelling analyses. At first, the results of the validation of the bone remodelling model are described. Then, the bone density distribution is evaluated qualitatively and quantitatively for the implanted bone with two implants, for both healthy and poor bone quality conditions.

In chapter 6, the results obtained are discussed and the main strengths and limitations of this study are presented.

In the last chapter, the major conclusions of this work are specified, along with future work suggestions that may complement this study.

Chapter 2

Background concepts

This chapter contains a brief introduction of the concepts involved in the context of the dissertation. To understand the biomechanical characteristics of the shoulder complex, a fundamental review of its anatomical and physiological features is presented. Besides that, the existing shoulder arthroplasty prostheses and component options are detailed, along with a literature review on the background of biomechanical modelling.

2.1 Key anatomical concepts

In order to promote a common understanding about the description of the human body throughout the world, it is important to become familiar with an internationally accepted vocabulary. In anatomy, the description of the human body is done regarding the anatomical reference position, illustrated in Figure 2-1. The position of anatomical structures is always described according to the reference position, regardless of the real position of the body when executing an action (Knudson, 2007; Palastanga & Soames, 2012).

To facilitate the spatial description of anatomical structures, three imaginary and perpendicular planes, depicted in Figure 2-1, are commonly used. The sagittal plane passes vertically from front to back, dividing the body into two symmetrical right and left segments. The coronal plane passes vertically from top to bottom, dividing the body into anterior and posterior sections. The transverse plane passes horizontally, dividing the body into superior and inferior sections. Furthermore, there are some common directional terms used to describe the position of structures concerning anatomical position: medial is used to locate a body part or motion toward the midline, while lateral refers to the opposite direction; anterior refers to parts positioned in the front of the body, whereas posterior refers to parts located in the back; superior and inferior are used to describe structures that are above or below another, respectively; and proximal and distal refer to the distance of a body part according to its closeness from the trunk (Knudson, 2007; Palastanga & Soames, 2012).

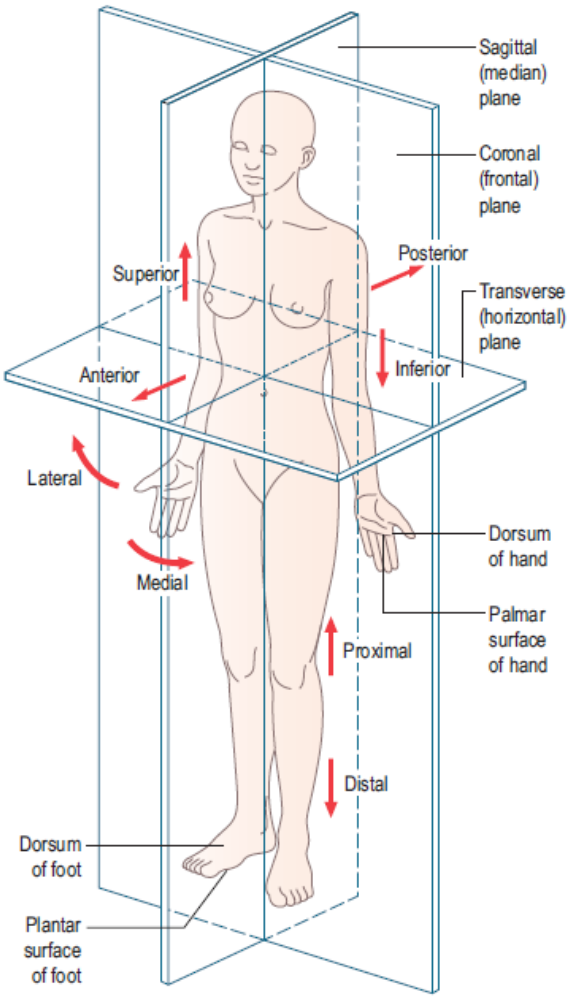

Figure 2-1 Anatomical reference position presenting the planes of motion and directional terminology (Palastanga & Soames, 2012).

2.2 Musculoskeletal system

The musculoskeletal system includes the skeletal, articular and muscular systems. A brief introduction of the structural and biomechanical information of the musculoskeletal system is provided next.

2.2.1 Skeletal system

The skeletal system is composed of bones; cartilages, which surround several joint surfaces in the mature skeleton; and ligaments, that maintain bones connected at the joints. The combination of these structures allows the body to form a strong and flexible framework, acting as a scaffold for the soft tissues by providing support and protection (Saladin et al., 2018). Besides the structural support and the protection of vital internal organs from injury, the skeletal wields other functions, such as: enabling body movement and locomotion by providing attachment points for muscles; preserving the mineral homeostasis and acid-base balance; providing a safe environment for blood cells formation; and maintaining an electrolyte balance

through the storage and release of calcium and phosphate ions, according to body's physiological needs (Clarke, 2008; Saladin et al., 2018).

2.2.1.1 Bone tissue

Bone is a specialized connective tissue containing a rich extracellular matrix, composed of about 25% water, 25% collagen fibers and 50% crystallized mineral salts, around a cellular component. The inorganic components confer hardness and rigidity to the bone while the organic component is responsible for bone's flexibility and resilience (Nordin & Frankel, 2001; Tortora & Derrickson, 2010).

Bone tissue exhibits four types of cells with unique functions: osteogenic, osteoblasts, osteocytes and osteoclasts. Osteogenic are unspecialized stem cells that have the capacity to differentiate and develop into osteoblasts, being the only bone cells capable of experiencing cell division. Osteoblasts are bone-forming cells that produce organic components necessary to build the bone extracellular matrix. Osteocytes are bone-maintaining cells. They are mature bone cells that derive from osteoblasts which have undergone changes in their structure after becoming trapped in the matrix they secreted. Osteoclasts are bone-resorbing cells that release enzymes and acids to digest protein and mineral components of the extracellular matrix, destroying it. They have the opposite function of osteoblasts, creating a balance on the bone tissue (Saladin et al., 2018; Tortora & Derrickson, 2010).

Bones are composed of two types of tissue, depending on its porosity and density: cortical or compact bone and trabecular or cancellous bone. Cortical bone has a dense, strong and tough structure that surrounds the marrow space and forms the hard outer shell of bones, making up 80% of the human skeleton (Tortora & Derrickson, 2010). It is organized in basic structural units known as osteons or haversian systems, illustrated in Figure 2-2 (a). Each osteon presents a cylindrical shape comprising layers of matrix concentrically organized around a central or haversian canal – concentric lamellae. The central canal encloses blood and lymphatic vessels, as well as nerves. There are small spaces between the lamellae named lacunae which contain osteocytes and where canaliculi can be found. Canaliculi are microscopic canals that create an extensive network, connecting lacunae with central canals and allowing for nutrients and oxygen to reach the osteocytes and for wastes to diffuse away for disposal. In contrast, trabecular bone is lighter than cortical bone, creating the spongy inner layer of bones composed of a network of trabeculae. Trabeculae is an irregular mesh structure composed of thin plates of bone filled with red bone marrow, which is the place of red and white bone cells formation (Nordin & Frankel, 2001; Saladin et al., 2018; Tortora & Derrickson, 2010). The relative quantity of each type differs according to functional requirements of each bone (Nordin & Frankel, 2001).

Bones vary widely in size and can be categorized into long, short, flat or irregular, based on their shape. A typical long bone, for instance, the humerus – shown in Figure 2-2 (b) –, has a cylindrical hollow central shaft called diaphysis, composed primarily of dense cortical bone. This shaft encloses a space named medullary cavity, filled with bone marrow. The diaphysis interconnects the proximal and distal

extremities of bone, referred as epiphysis. They are mainly composed of trabecular bone covered by a thin layer of cortical bone. Short bones are cube-shaped and are approximately similar in width and length. Flat bones are usually thin, grant large surfaces for muscle attachment sites and provide substantial protection to internal organs (Saladin et al., 2018; Tortora & Derrickson, 2010).

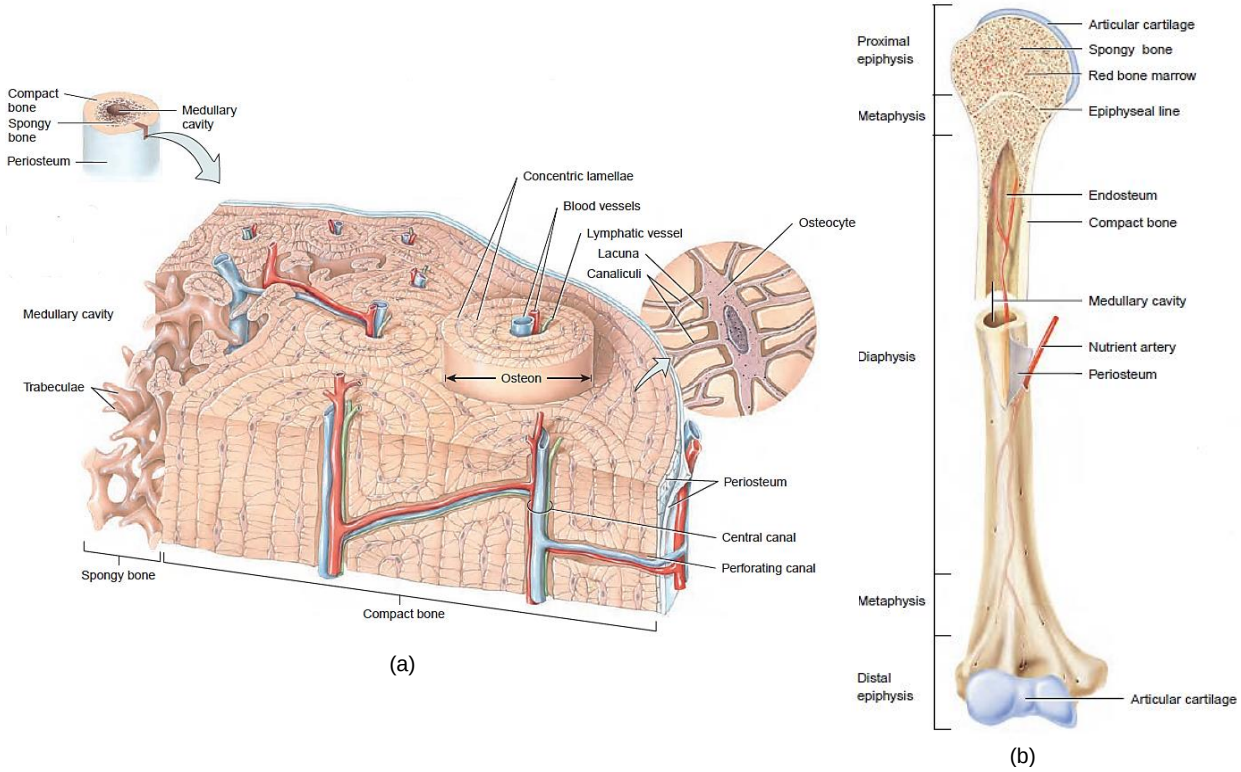

Figure 2-2 Microscopic and macroscopic structure of bone tissue. (a) Cortical and trabecular bone structure. (b) Partially sectioned humerus. (Adapted from Tortora & Derrickson, 2010)

2.2.1.2 Bone remodelling process

Bone tissue continuously renews itself throughout life as a result of a variety of stimuli by the process of bone remodelling, in which old bone is replaced by new bone in order to preserve bone strength and mineral stability. It requires a particular balance between bone deposition and resorption, by the combined action of osteoblasts and osteoclasts, respectively. This process prevents the accumulation of bone micro-damage, removing injured bone and reshaping bones in response to use and disuse (Clarke, 2008; Little et al., 2011; Saladin et al., 2018). Occasionally, an unbalance among the activity of bone cells leads to a series of skeletal disorders, such as osteoporosis. Osteoporosis is a common metabolic disorder of the skeleton that occurs when bone resorption exceeds its formation, resulting in a reduction of bone mass and strength which entails a higher susceptibility to fragility fractures (Rachner et al., 2011).

The occurrence of bone adaptation due to mechanical loads was first described by Wolff in the 19th century and is known as Wolff's law (Nordin & Frankel, 2001). According to Wolff, bone grows and remodels depending on the mechanical environment to which it is subjected. Therefore, whether a bone is heavily used or whether there is a permanently increased mechanical stress upon it, bone formation rises so that it can resist and become stronger. On the other hand, if the mechanical stress on the bone gradually decreases, bone resorption occurs due to the lack of stimulus, weakening the bone (Little et al., 2011; Saladin et al., 2018). Given that, in cases of extended periods of disuse and inactivity, for example, long-term bed rest and space travel or when prostheses are inserted into the bone, a significant bone mass' reduction is observed as a result of an adverse redistribution of stresses, which decreases bone's stimulus – phenomenon of stress shielding. Consequently, bone strength and stiffness also decrease (Nordin & Frankel, 2001).

2.2.2 Articular system

The joint is the fundamental structure of the articular system. It is the connection between bones or between cartilage and bones. Joints have different structures depending on their functional requirements. Tightly fitted joints allow minimal movement, thus being stronger and stable but less flexible. On the other hand, loosely fitted joints afford greater movement, therefore being more flexible but not as strong and stable. Joints movement depends on the shape of bones involved at the articular joint; on the flexibility of the ligaments that connect articulating bones; and on the tension of linked muscle and tendons (Marshall et al., 2014; Tortora & Derrickson, 2010).

Structurally, that is, based on their anatomical characteristics, joints can be classified into fibrous, cartilaginous and synovial joints. On fibrous and cartilaginous joints there is no synovial cavity and bones are bonded by dense irregular connective tissue rich in collagen fibers and cartilage, respectively, allowing only a limited amount of movement. As the name suggests, synovial joints present a space between the articulating bones, called synovial cavity; bones are held together by dense irregular connective tissue of an articular capsule and ligaments. The ligaments and joint capsule are crucial to the joint mechanical stability since they prevent joint's excessive motion without precluding a wide range of movement. Synovial joints comprise most of the joints from the upper and lower limbs. Functionally, i.e., based on the type of allowed movement, joints can be classified into synarthrosis, an immovable joint; amphiarthrosis, a slightly movable joint; and diarthrosis, a freely movable joint. All diarthroses are synovial joints (Tortora & Derrickson, 2010).

2.2.3 Muscular system

The muscular system is composed of three kinds of muscles: skeletal muscle, which attaches to the skeleton through tendons; cardiac muscle, which is found in the heart walls; and smooth muscle, which is found within the walls of hollow internal organs (Nordin & Frankel, 2001). In spite of their differences, all of

them have as their main purpose the conversion of chemical energy into mechanical energy to produce movement (Saladin et al., 2018).

The muscles integrated into the shoulder complex are from the skeleton type. By distributing loads and absorbing shock, skeleton muscles are responsible for the skeleton's protection while also providing strength to it. These muscles execute dynamic work by enabling the motion of the bones at the articulations and the positioning of the body parts in space, and they also allow static work by maintaining body posture.

2.3 The shoulder complex

The shoulder complex has an extreme importance on the general function of the upper limb. Together with the elbow motion, it allows precise positioning and complete use of the hand, with a range of motion higher than the needed to carry out daily activities (Culham & Peat, 1993; Wilk et al., 2009).

The skeletal segments of the shoulder complex are the humerus, the clavicle and the scapula. This complex is composed of three joints that function in a synchronized manner, connecting the upper extremity to the thorax: the glenohumeral joint, which links the humerus to the scapula; the acromioclavicular joint, which connects the clavicle to the scapula; and the sternoclavicular joint, which joins the upper extremity directly to the thorax. There is also the scapulothoracic "joint" which comprises the articulation between the scapula and the thorax. However, since this articulation does not have the characteristics of a fibrous, cartilaginous, or synovial joint, some authors do not consider it as a true anatomical joint of the shoulder complex (Levangie & Norkin, 2005). Considering that the components of the shoulder complex are connected to the trunk by a single joint, the sternoclavicular joint, the surrounding muscles have additional relevance since they provide a solid base of support for the movements of the upper extremities (Levangie & Norkin, 2005; Wilk et al., 2009).

The range of motion of the glenohumeral joint can be described using specific terms: flexion and extension refer to the anterior and posterior elevation of the arm in the sagittal plane, respectively; abduction and adduction refer to the lateral (away from the midline) or medial (toward the midline) elevation of the arm in the coronal plane, respectively; and medial (internal) and lateral (external) rotation refer to the rotation of the hand around the humeral vertical axis, with the elbow mid-flexed, toward the midline and away from the midline in the transverse plane, respectively (Nordin & Frankel, 2001; Singh, 2014; Tortora & Derrickson, 2010). The movements described above are represented in Figure 2-3.

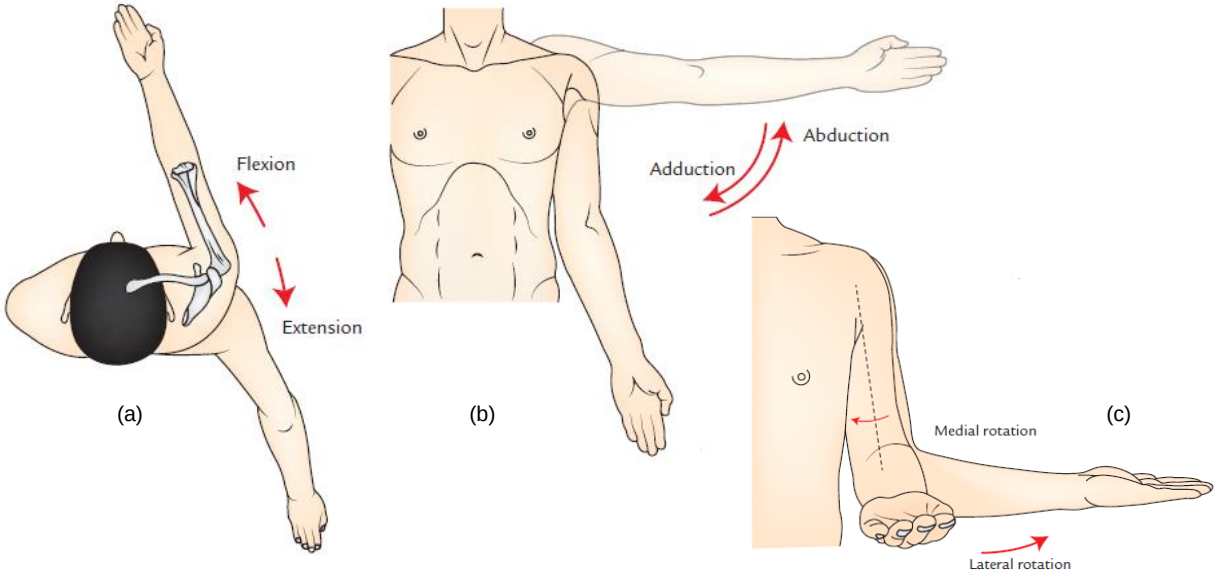

Figure 2-3 Movements of the glenohumeral joint. (a) Flexion and extension. (b) Abduction and adduction. (c) Medial and lateral rotation. (Singh, 2014)

2.3.1 Skeletal system

2.3.1.1 Humerus

The humerus, depicted in Figure 2-4, is a long bone and is the largest bone of the upper limb (Palastanga & Soames, 2012). Since the distal end is not relevant for the present work only the proximal extremity is described here.

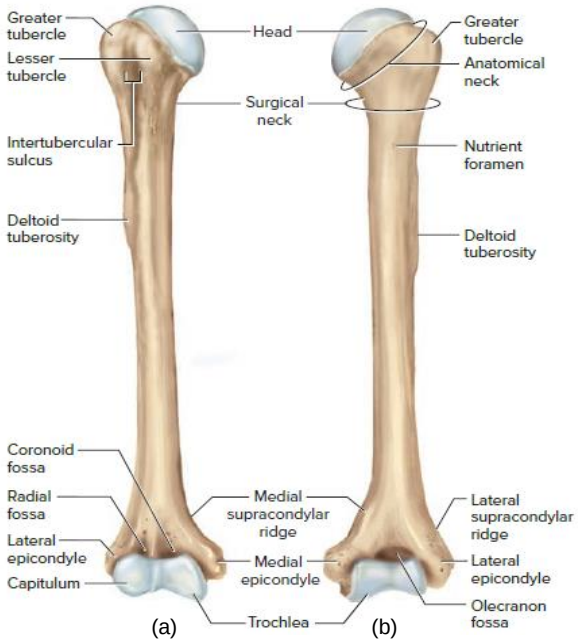

Figure 2-4 Right humerus. (a) Anterior view. (b) Posterior view. (Saladin et al., 2018)

The main feature of the proximal end of the humerus is the nearly hemispherical head which has a smooth and rounded surface that articulates with the glenoid cavity of scapula, establishing the glenohumeral joint. The head is directed medially, upwards and backwards, and is separated from the upper end of the diaphysis by the anatomical neck, which is a slightly constricted region encircling the bone at the articular margin (Palastanga & Soames, 2012). The tubercles, which are prominences that offer helpful support for shoulder muscle connections, are located below the anatomical neck. The greater tubercle is located at the upper lateral margin of the humerus and is the most lateral part of its proximal extremity, whereas the lesser tubercle is situated at the anterior aspect of the bone (Palastanga & Soames, 2012; Singh, 2014). Between the greater and lesser tubercle there is a deep intertubercular sulcus that lodges the tendon of the biceps muscle (Saladin et al., 2018). There is also a short constriction, the surgical neck, which is situated in the superior end of the diaphysis, below the tubercles at the transition from the head to the shaft. The surgical neck is a common fracture site, especially in elder individuals (Palastanga & Soames, 2012). On the lateral surface of the diaphysis, there is the deltoid tuberosity, which is an insertion site for the deltoid muscle (Saladin et al., 2018).

2.3.1.2 Scapula

The scapula, shown in Figure 2-5, is a large, flat, triangular bone located at the posterior section of the thorax, which covers the second to seventh ribs. The spine of the scapula extends diagonally across its posterior surface. The lateral end of the spine, commonly known as acromion, is the location of the articulation between the scapula and clavicle, known as acromioclavicular joint. Beneath the acromion, there is a depression named glenoid cavity or fossa, which articulates with the humeral head forming the glenohumeral joint (Tortora & Derrickson, 2010). Superiorly, in the anterolateral section of the scapula is situated the coracoid process. It is a hook-like projection that provides an attachment site for tendons of the biceps brachii as well as other arm muscles (Palastanga & Soames, 2012; Saladin et al., 2018).

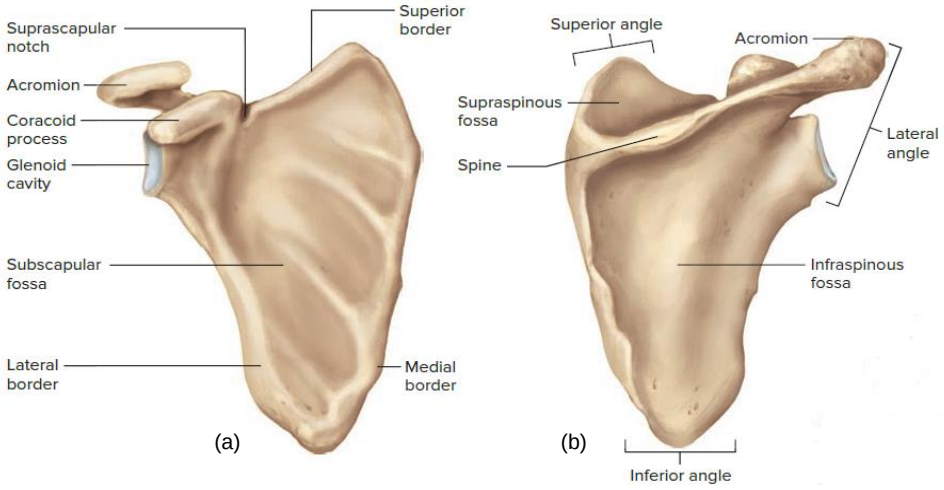

Figure 2-5 Right scapula. (a) Anterior view. (b) Posterior view. (Saladin et al., 2018)

2.3.1.3 Clavicle

The clavicle, shown in Figure 2-6 is a long, slight S-shaped bone situated horizontally above the first rib. Its medial extremity articulates with the sternum at the sternoclavicular joint and the lateral extremity with the scapula at the acromioclavicular joint. Both scapula and clavicle form the pectoral or shoulder girdle, which attaches the bones of the upper limb to the axial skeleton (Tortora & Derrickson, 2010).

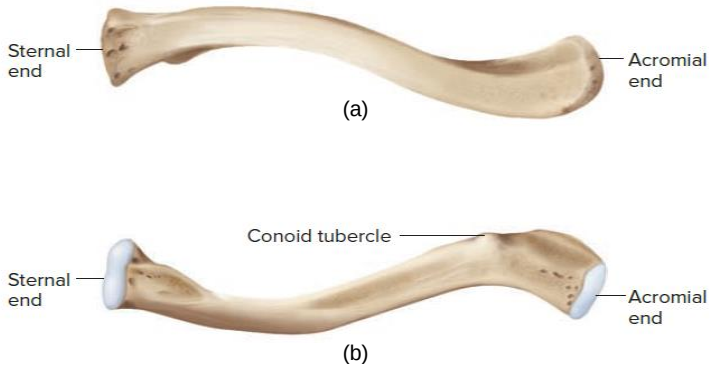

Figure 2-6 Right clavicle. (a) Anterior view. (b) Posterior view. (Saladin et al., 2018)

2.3.2 Articular system – glenohumeral joint

The glenohumeral joint, illustrated in Figure 2-7, is the articulation between the head of the humerus and the glenoid cavity of the scapula and it is the joint that presents the biggest range of motion in the human body. It is a ball-and-socket type of synovial joint with the head of the humerus acting as the ball and the glenoid cavity as the socket (Singh, 2014). Both humeral head and glenoid cavity are covered with hyaline cartilage.

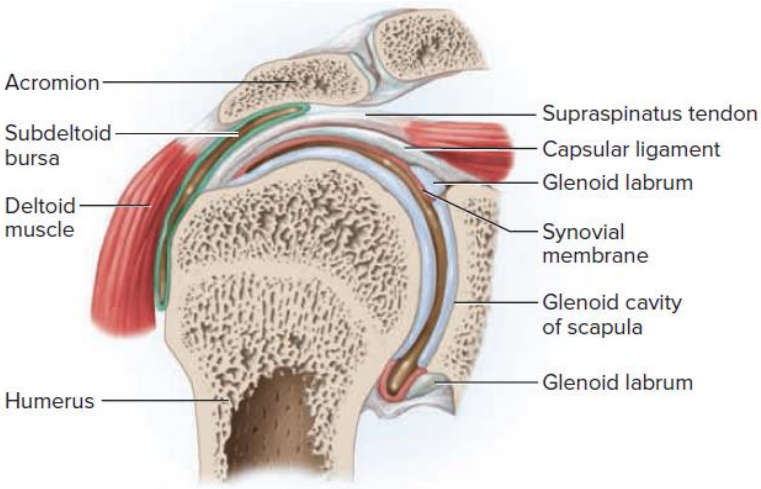

Figure 2-7 Frontal view of the glenohumeral joint. (Saladin et al., 2018)

The head of the humerus represents two-fifths of a sphere (Palastanga & Soames, 2012) and the articular surface has a radius of curvature of 35 to 55 millimetres (Wilk et al., 2009). Together with the humeral neck, the head makes an angle of 135 to 140 degrees with the axis of the shaft in the frontal plane – angle of

inclination –, and is rotated backwards about 30 to 40 degrees against the shaft – angle of retroversion (Palastanga & Soames, 2012). These two angles are shown in Figure 2-8. Since the humeral head is larger than the glenoid fossa, only one-third of the former is in contact with the latter (Levangie & Norkin, 2005; Palastanga & Soames, 2012). Despite leading to a flawed adjustment and inherent instability, which increases the chance of injuries and dislocations, this configuration enables an astounding amount of motion (Levangie & Norkin, 2005).

Considering the lack of bone restrictions, joint stability is accomplished by the capsular, ligamentous and muscular structures that enclose the glenohumeral joint (Nordin & Frankel, 2001). The glenoid labrum, joint capsule and ligaments are considered static stabilizers, whereas muscles are considered dynamic stabilizers.

The glenoid labrum is a rim of fibrocartilaginous tissue that surrounds and is attached to the margin of the glenoid fossa, enhancing the depth of curvature of the fossa by 50% (Nordin & Frankel, 2001; Wilk et al., 2009). It acts as an attachment for the glenohumeral ligaments (Wilk et al., 2009).

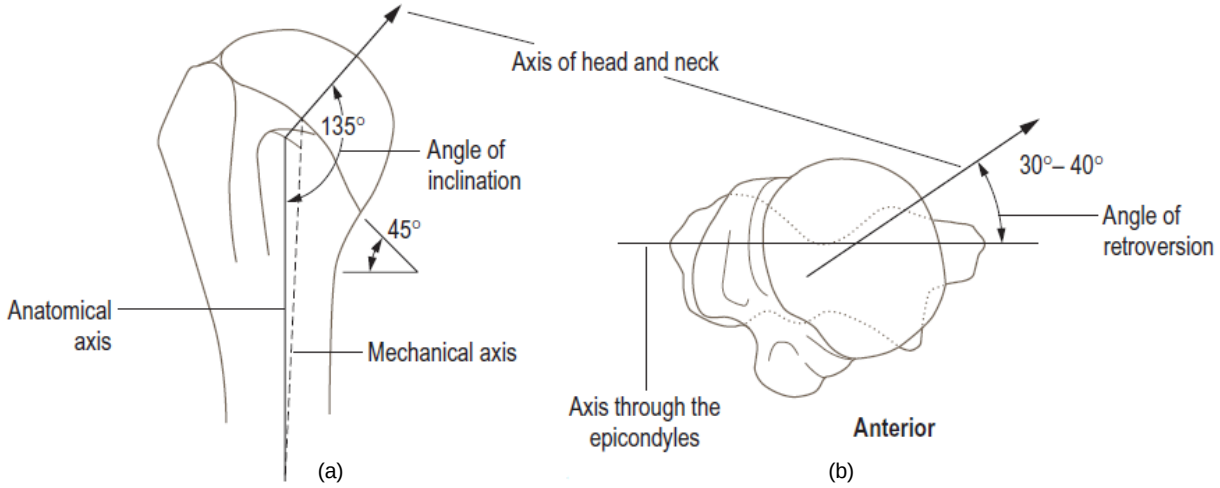

Figure 2-8 The angle of (a) inclination and (b) retroversion of humerus. (Palastanga & Soames, 2012)

The fibrous joint capsule encircles the articulation and has a surface area twice as big as the surface of the humeral head (Nordin & Frankel, 2001). This allows a significant degree of mobility due to its loose-fitting structure, but adds little stability to the joint. For that reason, the reinforcement of the capsule by ligaments and muscle tendons is crucial to its integrity (Wilk et al., 2009). On the scapula, the capsule is attached to the labrum superiorly and posteriorly, and beyond the glenoid labrum anteriorly and inferiorly. On the humerus, the capsule attaches to the circumference of the anatomical neck (Palastanga & Soames, 2012; Wilk et al., 2009). Despite its reduced contribution, the capsule has a stabilizing role in different arm positions. In adduction, the capsule is taut superiorly and relaxed inferiorly while the opposite is verified in

abduction. In lateral rotation the anterior capsule tightens and the posterior capsule relaxes whereas in medial rotation it is the other way around (Nordin & Frankel, 2001).

On the anterior aspect of the joint, the capsule is thickened and reinforced by three glenohumeral ligaments: superior, middle and inferior glenohumeral ligaments. These ligaments have different functions and are illustrated in Figure 2-9. The superior glenohumeral ligament constitutes the fundamental restriction to inferior translation with the arm in the adducted position, whereas the middle glenohumeral ligament constitutes the secondary constraint to inferior translation with the arm in the abducted and externally rotated position and also as a constraint to anterior translation. The inferior glenohumeral ligament is divided into three distinct components, acting as the primary anterior stabilizer of the shoulder with the arm abducted 90º and as a restraint to inferior translation with the arm in the abducted position. The superoposterior aspect of the joint is strengthened by the coracohumeral ligament which strengthens the superior aspect of the joint capsule (Nordin & Frankel, 2001; Palastanga & Soames, 2012).

The glenohumeral joint is surrounded by muscles that connect the scapula and the clavicle with the humerus. They are aimed to protect the joint by assisting in the support of the upper limb. The anterior section of the articulation is associated with the tendon of the subscapularis muscle, the superior section with the tendon of the supraspinatus muscle and the posterior section with the tendons of the infraspinatus and teres minor muscles. These tendons known as rotator cuff, act as stretchable ligaments and merge with the capsule of the shoulder joint, reinforcing it by holding the humeral head against the glenoid cavity of scapula. Their insertion is located on the proximal end of the humerus, where tendons bend together and form a partial sleeve around the capsule (Saladin et al., 2018; Singh, 2014); The rotator cuff muscles play an essential role in preserving the integrity of the joint (Palastanga & Soames, 2012). Besides helping in stabilization, muscles are crucial for joint mobility. Apart from the rotator cuff muscles, pectoralis major, latissimus dorsi, deltoid, teres major and coracobrachialis muscles also contribute to the motion of humerus.

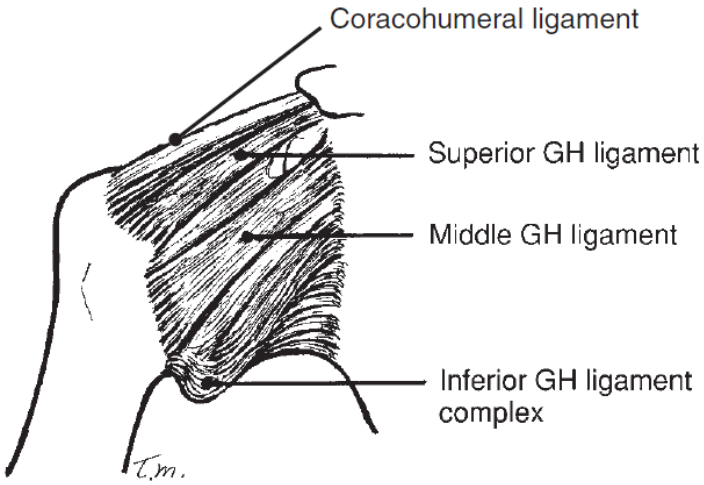

Figure 2-9 Coracohumeral and glenohumeral ligaments that reinforce the shoulder joint capsule (Levangie & Norkin, 2005).

In order to increase the glenohumeral joint stability, there are other constraints that should be considered, specifically the adhesion-cohesion and the negative intra-articular pressure mechanisms. The synovial fluid acts by means of the adhesion-cohesion mechanism. It adheres to the articular cartilage covering the humeral head and the glenoid, allowing both joint surfaces to slide on each other, whilst exerting cohesive forces between the surfaces. Under normal conditions, the joint capsule seals the glenohumeral joint creating a negative intra-articular pressure which holds the joint together. If the integrity of the joint capsule is jeopardized, not only by its venting but also by a significant outflow of fluid, the resistance to displacement decreases and significant increases in translation are detected (Nordin & Frankel, 2001).

2.3.3 Shoulder muscles

Nine muscles with attachment sites on the humerus span the glenohumeral joint. Two of them, the pectoralis major and the latissimus dorsi, have their origin in the axial skeleton, and thus are considered axial muscles. The remaining seven muscles originate on the scapula and are known as scapular muscles: deltoid, teres major, coracobrachialis and the rotator cuff muscles – supraspinatus, infraspinatus, teres minor and subscapularis (Saladin et al., 2018; Tortora & Derrickson, 2010).

In addition to the rotator cuff muscles, two other muscles have an important role in the function of the shoulder joint, namely the biceps brachii and the triceps brachii muscle, by increasing its stabilization. The long head of biceps brachii muscle passes inside the capsule above the humeral head, bracing it against the glenoid and thus preventing its upward displacement (Palastanga & Soames, 2012; Singh, 2014).

Table 2-1 summarizes the attachment sites and the action of muscles relevant for the characterization of the mechanical environment of the shoulder joint. Figures 2-10 and 2-11 illustrate the muscles of Table 2-1.

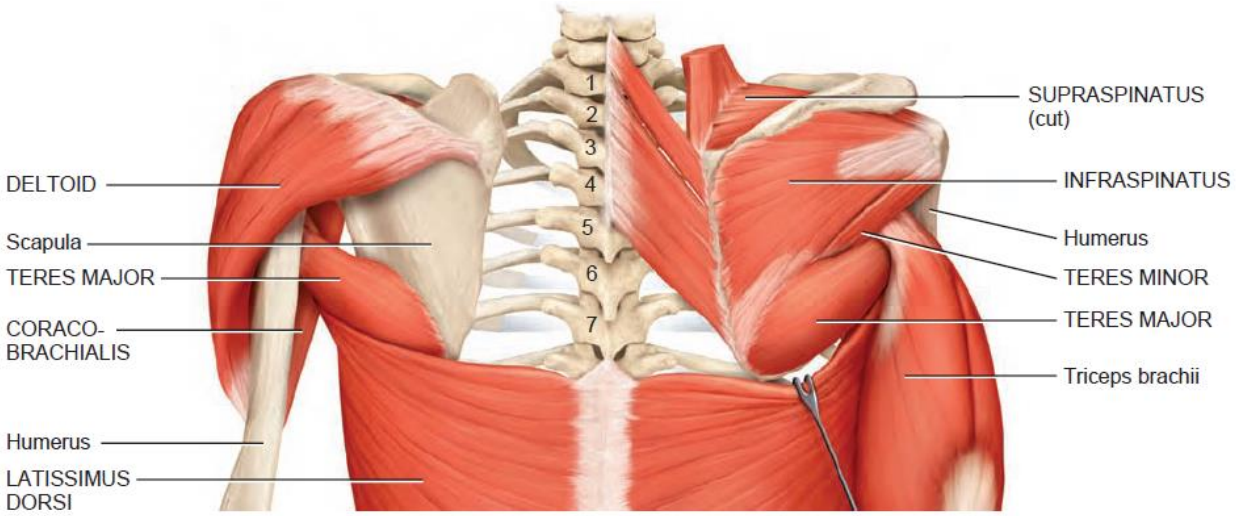

Figure 2-10 Posterior view of the muscles of the thorax and shoulder responsible for the humerus movement (Tortora & Derrickson, 2010).

Table 2-1 Description of the attachment sites and action of the muscles that best characterize the mechanical environment of the shoulder joint (Adapted from Tortora and Derrickson, 2010; Singh, 2014; Saladin, Gan and Cushman, 2018).

Muscle	Origin	Insertion	Action
Pectoralis major	Medial half of clavicle, lateral margin of sternum, cartilages of second to sixth ribs	Lateral lip of intertubercular sulcus of humerus	Adducts and rotates arm medially at shoulder joint; flexes and extends arm at shoulder joint
Latissimus dorsi	Spines of lower six thoracic vertebrae, lumbar vertebrae, sacrum, and ilium, lower four ribs	Floor of intertubercular sulcus of humerus	Extends, adducts, and rotates arm medially at shoulder joint; draws arm downward and backward
Deltoid	Acromion and spine of scapula, clavicle	Deltoid tuberosity of humerus	Abducts, flexes, extends, and rotates arm at shoulder joint
Subscapularis	Suprascapular fossa of scapula	Lesser tubercle of humerus	Rotates arm medially at shoulder joint
Supraspinatus	Supraspinous fossa of scapula	Superior facet of greater tubercle of humerus	Assists deltoid muscle in abducting arm at shoulder joint
Infraspinatus	Infraspinous fossa of scapula	Middle facet of greater tubercle of humerus	Rotates arm laterally at shoulder joint
Teres major	Inferior angle of scapula	Medial lip of the intertubercular sulcus of humerus	Extends arm at shoulder joint; assists in adduction and rotation of arm medially at shoulder joint
Teres minor	Lateral border and adjacent posterior surface of scapula	Inferior facet of greater tubercle of humerus	Rotates arm laterally and extends arm at shoulder joint
Coracobrachialis	Coracoid process of scapula	Medial aspect of humeral shaft	Flexes and adducts arm at shoulder joint
Biceps brachii	Long head: superior margin of glenoid cavity Short head: tip of the coracoid process	Radius	Flexes and supinates forearm at elbow joint; flexes arm at shoulder joint
Triceps brachii	Long head: inferior margin of glenoid cavity and joint capsule Lateral head: posterior surface of proximal end of humerus Medial head: posterior surface of entire humeral shaft	Ulna	Extends forearm at elbow joint; extends arm at shoulder joint

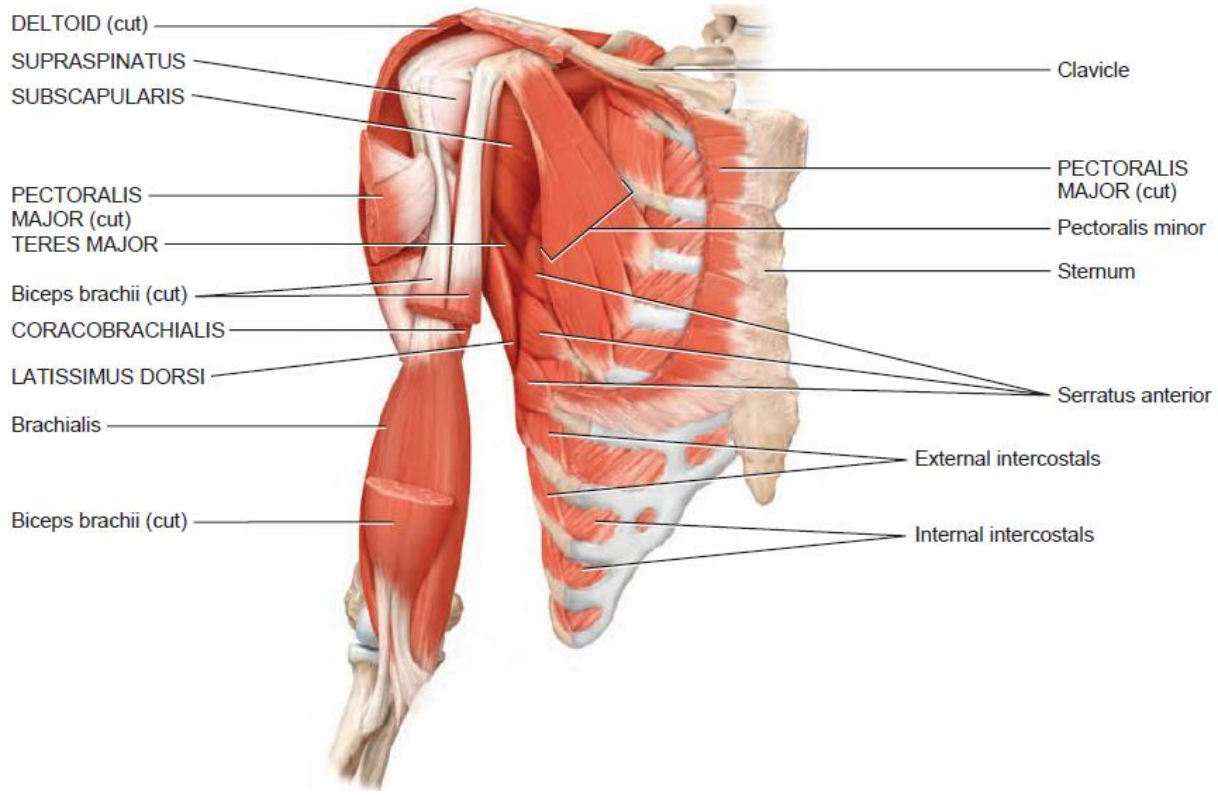

Figure 2-11 Anterior deep view of the muscles of the thorax and shoulder responsible for the humerus movement (Tortora & Derrickson, 2010).

2.4 Shoulder Arthroplasty

The shoulder arthroplasty is a surgical procedure for the treatment of primary and secondary degenerative pathologies of the shoulder joint. It restores the mobility and function of the joint and relieves shoulder pain (Quental, Folgado, et al., 2014). In the last few years, shoulder arthroplasty has increased its popularity among the orthopaedic community. Its indications and use have been growing so much that new implant designs are continuously being developed (Boileau et al., 2006; Sanchez-Sotelo, 2011; Sheridan et al., 2012).

The first reported shoulder arthroplasty dates back to 1893 when the French surgeon Jules-Émile Péan implanted a platinum and rubber humeral prosthesis to replace a glenohumeral joint destroyed by tuberculosis. Due to chronic infection, the prosthesis was removed two years later. Although the credit of performing the first shoulder arthroplasty is given to Péan, evidences suggest that it was Themistocles Gluck who first designed an ivory shoulder replacement. However, there is no report that it was ever implanted (Gartsman & Edwards, 2008; Sheridan et al., 2012).

In the 1950s the modern era of shoulder arthroplasty emerged through the work of Charles S. Neer II. At first, Neer developed a cobalt alloy monoblock prosthesis for the treatment of proximal humeral fractures, commonly known as first-generation of shoulder prostheses. However, dissimilarities among patients in

respect to humeral head sizes instigated the evolution of his original designs towards modularity. The second generation of shoulder prostheses appeared with the introduction of modular humeral head with modifiable diameter, allowing a better replication of the shoulder anatomy (Gartsman & Edwards, 2008; Sheridan et al., 2012). Several studies evaluating the relative variability of certain anatomical parameters promoted the development of new-generation humeral component designs, commonly referred to as adaptable and modular (Gartsman & Edwards, 2008; Petriccioli et al., 2015). In 1974, Neer combined a redesigned humeral implant with a polyethylene glenoid resurfacing component for the treatment of glenohumeral osteoarthritis, which gave rise to total shoulder arthroplasty (Churchill, 2014; Wiater & Fabing, 2009). Also in the 1970s, as a result of the failure of non-constrained prostheses in patients with pain and limited function resulting from rotator cuff deficiency, the fixed-fulcrum constrained reverse shoulder prostheses emerged. However, their design characteristics led to an early mechanical failure and they were abandoned. Notwithstanding, the principles of the reverse shoulder arthroplasty were created (Katz et al., 2007; Wiater & Fabing, 2009). Since Neer's original design, over 70 different shoulder prostheses have been developed (Sheridan et al., 2012; Wiater & Fabing, 2009).

2.4.1 Types of shoulder replacement

Nowadays, the shoulder replacement can be categorized into two main types: anatomical shoulder arthroplasty and reverse shoulder arthroplasty, which are illustrated in Figure 2-12. The anatomical shoulder arthroplasty can be divided into total shoulder arthroplasty (TSA), which involves the replacement of both humeral head and glenoid articular surfaces by an implant, and hemiarthroplasty, that only involves the replacement of the articular surface of the humeral head by an implant. The reverse shoulder arthroplasty, commonly known as reverse total shoulder arthroplasty (RTSA), shifts the normal anatomy of the glenohumeral joint through the use of a semi-constrained prosthesis. In other words, the socket is attached to the humerus and the ball is attached to the scapula. Factors such as the age of the patient and his activity level, the extent of wear to both humeral head and glenoid, and the functional condition of rotator cuff must be considered when choosing the appropriate replacement option (Sheridan et al., 2012).

Typically, the hemiarthroplasty is indicated in arthritic conditions, when the glenoid bone stock is insufficient to support a glenoid prosthesis; after a severe proximal humerus fracture or in early stages of osteonecrosis of the proximal humerus, if the glenoid is intact; or when there is a serious risk of glenoid wear and loosening in active young patients with osteoarthritis (Boileau et al., 2006; Sheridan et al., 2012). TSA is designated for patients with an intact and functioning rotator cuff. The primary indication for TSA is a glenohumeral osteoarthritis condition that is unresponsive to nonsurgical treatment, together with loss of articular cartilage in patients with adequate glenoid bone stock. Other indications include inflammatory arthritis; osteonecrosis with glenoid involvement; and posttraumatic degenerative joint disease (Sheridan et al., 2012; Wiater & Fabing, 2009). The main indication for RTSA is cuff tear arthropathy. Recently, its use has increased for the treatment of four-part fracture dislocations of the

proximal humerus in osteoporotic bone; revision shoulder arthroplasty; and rotator cuff failure associated with glenohumeral instability (Sheridan et al., 2012). Initially the RTSA was indicated only for older patients but, over the years, it is becoming more common in younger patients as an alternative to hemiarthroplasty, despite the limited information about its long-term results (Sanchez-Sotelo, 2009).

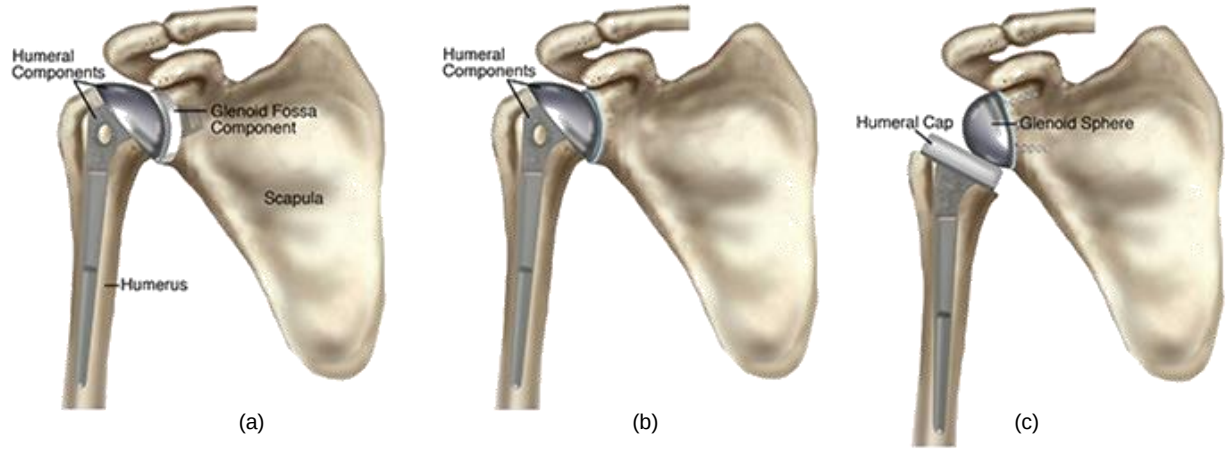

Figure 2-12 Types of shoulder replacement. (a) Total shoulder arthroplasty. (b) Hemiarthroplasty. (c) Reverse total shoulder arthroplasty ("Total Shoulder Replacement (Arthroplasty)", n.d.).

In the literature, there is still some controversy regarding which anatomical procedure, hemiarthroplasty or TSA, is better. However, the debate occurs mainly for the treatment of primary osteoarthritis. Some studies have shown that in osteoarthritis TSA is superior to hemiarthroplasty in terms of pain relief, functional outcome and patient satisfaction, along with a lower rate of revision surgery (Boileau et al., 2006; Wiater & Fabing, 2009). However, although TSA suggests better short and mid-term results, it also presents a risk of long-term problems related to the glenoid component, such as loosening (Boileau et al., 2006; Somerson et al., 2016).

In the past few years, the number of implemented shoulder arthroplasties has grown significantly, creating an increased need for revision surgery. Component loosening, from both humerus and glenoid, is the main complication of anatomical shoulder arthroplasty (Bohsali et al., 2017). Besides loosening, the most common complications following a shoulder arthroplasty include glenoid wear; instability; rotator cuff tear; intraoperative and postoperative periprosthetic fracture; neural injury; infection; hematoma; deltoid injury; and venous thromboembolism (Bohsali et al., 2017). These complications are more or less transversal to all replacement options, yet with distinct frequencies.

2.4.2 Shoulder components options

There are several options for both glenoid and humeral components within the different types of shoulder replacement. However, it is worth mentioning that RTSA requires the use of particular components due to its non-anatomical geometry that will not be discussed in this work (Sheridan et al., 2012). The available

prostheses in the market allow multiple configurations to allow their adaptation, in the best way possible, to the anatomy of each patient.

The glenoid component, only used in TSA, can be an all-polyethylene component, which consists of a cup fixed by cementing techniques with a keel or a peg; or a metal-backed component, which consists of a polyethylene cup inserted into a metal shell that can be fixated by screws or press-fit, commonly made from titanium alloys. Most of the metal-backed components are coated with hydroxyapatite to promote osseointegration (Sheridan et al., 2012).

Currently, there are three options for the humeral component: stemmed humeral replacement, humeral resurfacing and stemless humeral replacement. All of the humeral components described below can be used in TSA, together with a glenoid component, or in hemiarthroplasty.

Stemmed humeral replacement requires the resection of the humeral head and relies on metaphyseal and diaphyseal fixation. The stabilization of the implant can be accomplished by biological fixation with an uncemented “press-fit” or by mechanical fixation with cement. Recent modular designs allow customization of the head inclination, translation and version as well as multiple stem lengths and diameters to pair with variable head sizes (Sheridan et al., 2012).

In long-term results, humeral stems have raised some concerns such as proximal humeral bone resorption due to stress shielding; humeral stem loosening; and osteolysis, which is bone’s immunological response to wear particles released into the joint that results in its resorption. Moreover, removal of a well-fixed humeral stem in revision arthroplasty can be challenging, resulting in further proximal bone destruction. Thus, shortening of the stem as well as cementless application techniques that preserve the proximal bone stock have arisen to reduce humeral stem complications (Churchill, 2014; Churchill & Athwal, 2016).

Humeral resurfacing is a possible alternative to conventional stemmed humeral replacement, especially in young patients. It relies on the preservation of most part of the humeral head, by replacing the joint surface with a metal cap, thus restoring the normal anatomy of the humerus with minimal bone resection. Regarding the procedure, the existing osteophytes of the arthritic humeral head are removed; the head is then reamed to the appropriate size; and at last a cap is placed, covering the existing head (Sheridan et al., 2012). Initial stabilization is accomplished with press-fit fixation. Then, bone ongrowth is reassured by a hydroxyapatite or ceramic porous coating (Sheridan et al., 2012). Current designs have a central humeral stem, which can vary in shape, diameter and length. Most humeral resurfacing components are made of cobalt-chromium alloy and, less frequently of titanium alloy. The advantages of humeral resurfacing over the stemmed humeral replacement are a decreased bone resection with no need to perform osteotomy; shorter operative times; a lower prevalence of humeral periprosthetic fractures; and an ease of revision to a stemmed replacement, if needed. The disadvantages are the limited ability to correct for lateralization of the glenoid and the impossibility of lowering the humeral offset by decreasing

the head and neck length, since no osteotomy is performed (Burgess et al., 2009). An example of a stemmed humeral implant and a humeral resurfacing implant is illustrated in the cross-sectional scheme of Figure 2-13.

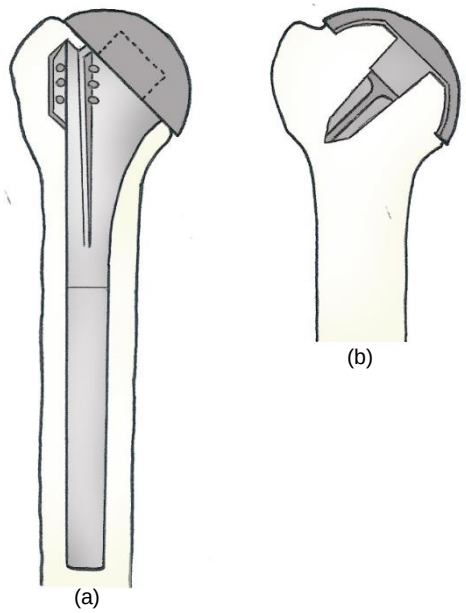

Figure 2-13 Cross-sectional scheme of (a) a stemmed humeral implant and (b) a humeral resurfacing implant.

Humeral resurfacing has demonstrated low complication rates in studies with follow-up times between eight months to seven years (Burgess et al., 2009). Besides that, the revision rates of both resurfacing and stemmed prosthesis appear to be comparable, or even better, in the case of the humeral resurfacing (Burgess et al., 2009; Levy, 2016). On the other hand, when comparing TSA and hemiarthroplasty with resurfacing, Levy et al. (2010) reported very little difference in pain and functional outcome. Moreover, this study revealed longer survivorship of hemiarthroplasty than TSA resurfacing prostheses with 95.8% (92.3% to 99.3%) and 89.7% (84.0% to 95.5%), respectively.

Over the past decade, the stemless humeral replacement has emerged with the intention of completely avoiding stem related complications, providing ease of revision and maintaining bone quality in revision arthroplasties. In contrast to humeral resurfacing, which preserves the majority of the humeral head, stemless humeral replacement relies on metaphyseal fixation and mid-head resection, allowing a full exposure and optimal access for glenoid replacement while minimizing humeral bone removal (Churchill, 2014; Churchill & Athwal, 2016; Petriccioli et al., 2015). The humeral head is resected as performed for a stemmed prosthesis, but diaphyseal preparation is not required. After resecting the humeral neck, a metaphyseal base plate is inserted, which can be anchored by impaction or with a large diameter screw. Finally, the base plate is fixed through press-fit to the humeral head. The anchor, i.e., the back of the base plate, is coated to facilitate bone ingrowth or ongrowth, depending on the implant (Sheridan et al., 2012). Implant's specific design features such as insertion technique, presence or absence of a collar, surface

coating, and low or high bone contact area have to be considered when assessing stemless implant stability. By the published reports of stemmed replacements over the years, it is known that slight differences in implant designs can have a tremendous effect on clinical and radiographic outcomes (Churchill & Athwal, 2016). The cross-sectional schemes of three kinds of stemless humeral implants are illustrated in Figure 2-14.

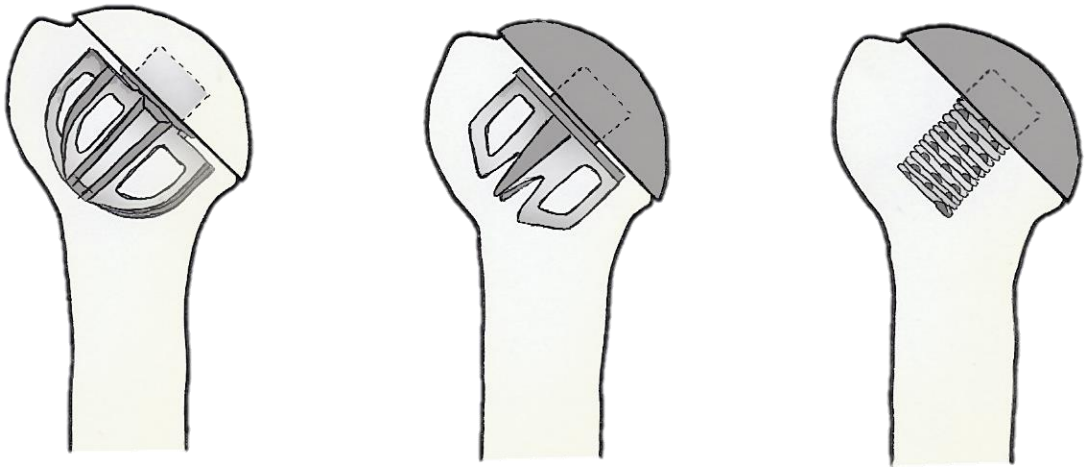

Figure 2-14 Cross-sectional scheme of three types of stemless humeral implants.

A few clinical studies indicate that stemless humeral replacement has short and midterm results similar to stemmed replacement (Churchill, 2014; Churchill & Athwal, 2016). However, the numerous implant designs available present significant variations, making impossible to predict whether a stemless implant will be successful or not. Besides that, only three of the eight available stemless designs have the required follow-up study of 2 years or more. Given the lack of existing literature, careful consideration of clinical results has to be taken before drawing premature conclusions about the technique.

2.5 Background on biomechanical modelling

Over the last few decades, an increasing interest regarding how different structures of the human body adapt to various mechanical conditions has led to the development of progressively sophisticated biomechanical numerical models. Throughout simulation, these models allow the analysis of complex biological aspects without the need of in-vivo experiments (Favre et al., 2009).

Finite element models are a type of biomechanical models that have been widely used to study the effect of load transfer in bone morphology by estimating the changes in stress and strain distributions (Poelert et al., 2013). Finite element (FE) analyses are performed on orthopaedic devices to assist in the design and pre-clinical investigation of new implants; to evaluate the initial post-op mechanical environment by the simulation of time dependent processes, such as bone remodelling; and, more recently, to guide the orthopaedic surgeons in the decision making process (Taylor & Prendergast, 2015). With the advance in imaging modalities techniques, subject-specific finite element models have emerged and have been

increasingly used by surgeons in pre- and intraoperative planning of implant placement (Poelert et al., 2013). Due to the high computational cost associated with FE analyses, models are usually simplified by focusing only on a specific part of the human body (Favre et al., 2009). Regarding the shoulder joint, most studies have investigated the biomechanics of the scapula, since one of the major complications of the TSA is the loosening of the glenoid component (Bohsali et al., 2017; Zheng et al., 2017). FE models have been widely used to investigate the mechanical factors related to component fixation and loosening by the influence of implant component's shape and type and also by design parameters (Friedman et al., 1992; Lacroix et al., 2016; Schmidutz et al., 2014; Stone et al., 1999). Another aspects that have been studied are the type of fixation techniques of the prostheses, i.e., cemented or uncemented (Gupta et al., 2004; Gupta & Dan, 2004) and the implant positioning on bone (Hopkins et al., 2004).

In literature, few finite element studies address the resurfacing implants and only recently has the stress shielding phenomenon been evaluated by Schmidutz et al. (2014). In this study, the changes in bone compressive strains where estimated before and after a shoulder arthroplasty with two different resurfacing implants. The attempt to reduce the stem-related complications associated with shoulder arthroplasty has led to the design of stemless implants. These implants have been introduced in the clinics recently, so the available knowledge on their primary stability is reduced. In an attempt to revert this situation, Favre & Henderson (2016) have evaluated the micromotion of a stemless humeral implant during several upper limb activities. Also, a study of Razfar et al. (2015) suggests that potential stress shielding in the proximal humerus may be reduced by the use of shorter stems.

Bone remodelling models have been used to simulate the bone adaptation to the mechanical environment using finite element models. Although most simulations have focused on the hip and knee (Behrens et al., 2009; P. R. Fernandes et al., 2002; Geraldes et al., 2016; Quilez et al., 2017; Ruben et al., 2012), recently they have also been applied to the shoulder joint in both scapula (Quental, Fernandes, et al., 2014; Sharma et al., 2010; Sharma & Robertson, 2013; Suárez et al., 2012) and humerus (Quental et al., 2012). Although the adaptation process of the humerus with stemmed cemented and cementless implants has been addressed by Quental et al. (2012), as far as the author knows, there are no studies evaluating the bone remodelling process in resurfacing and stemless implants of the shoulder joint. In the hip, the resurfacing implants have been already assessed regarding the bone adaptation simulation (Behrens et al., 2009; Gupta et al., 2006; Rothstock et al., 2011).

The aim of the present work is to provide valuable information in the understanding of how the humerus adapts to specific resurfacing and stemless implants after a shoulder arthroplasty, through the numerical simulation of bone remodelling using the finite element analysis. These two types of implants are believed to be the future of shoulder arthroplasty; however, there is still lack of knowledge about the potential long-term complications associated with them.

Chapter 3

Bone remodelling model

Computational models of bone remodelling are important tools to understand the bone adaptation process from the mechanical point of view. These models are able to predict the behaviour of the bone when subjected to specific load conditions, for instance, in the presence of an orthopaedic implant. The bone remodelling model applied in this work was developed by Fernandes et al. (1999), who proposes a three-dimensional optimization model for bone adaptation. This model is centred on Wolff's original ideas, particularly on the trajectorial theory of trabecular orientation, which proposes that morphogenic processes, such as bone growth and fracture healing, produce trabeculae aligned with directions of the principal stresses. Thus, Fernandes et al. (1999) consider bone as a material with orthogonal microstructure which can change its bone density and orientation in response to the mechanical environment. A brief description of the material model, optimization problem and numerical simulation is presented in this chapter.

3.1 Material model

Bone is modelled as a linearly elastic porous material with a periodic microstructure. The microstructure is obtained by the repetition of cubic unit cells with rectangular holes, known as open cell (Folgado et al., 2004), with dimensions a_1, a_2 and a_3. These dimensions allow the simulation of different levels of porosity. Moreover, the porous material is considered orthotropic, allowing the simulation of bone as an oriented material.

At each point, bone is characterized through a local microstructure, as shown in Figure 3-1, in which its relative density and orientation are defined by the parameters $\boldsymbol{a} = [a_1, a_2, a_3]^T$ and by the Euler angles $\boldsymbol{\theta} = [\theta_1, \theta_2, \theta_3]^T$, respectively. The relative density is given by

$$\rho = 1 - a_1 a_2 - a_1 a_3 - a_2 a_3 + 2 a_1 a_2 a_3, \tag{3-1}$$

with $a_i \in [0,1]$ and $i = 1,2,3$. The limit values $a_i = 0$ and $a_i = 1$ correspond to compact bone and void, respectively.

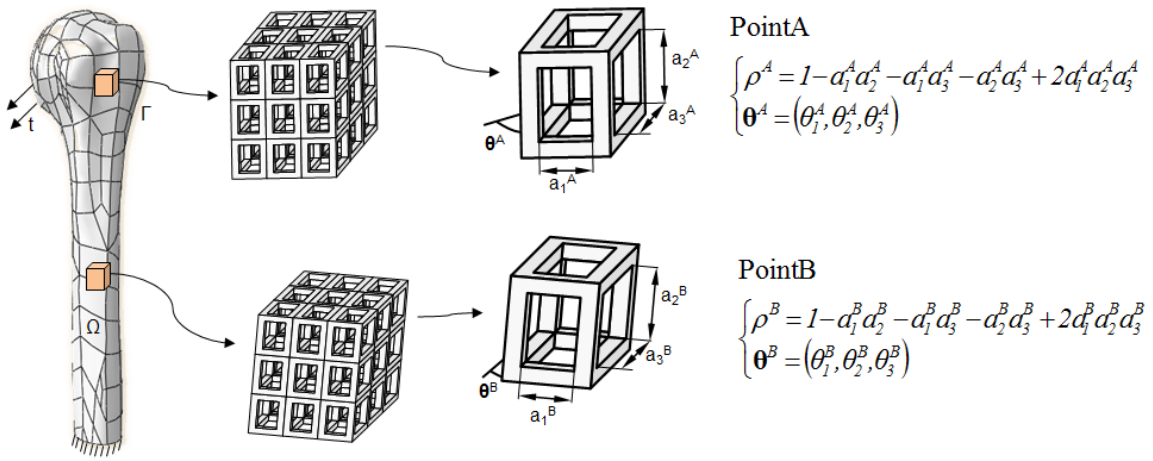

Figure 3-1 Material model of bone (Quental, 2013)

The elastic properties of bone are computed using the homogenization method, which is fully described in (Guedes & Kikuchi, 1990). This method computes equivalent homogenised material properties for the locally periodic porous material with similar microstructure. Assuming compact bone as the base material, the homogenized material properties E_{ijkm}^H are obtained by

$$E_{ijkm}^H = \frac{1}{|Y|}\int_{Y^*}\left(E_{ijkl} - E_{ijpm}\frac{\partial \chi_p^{kl}}{\partial y_m}\right)dy, \qquad (3\text{-}2)$$

where Y represents the domain of the unit cell, and Y^* represents its solid part, E_{ijkl} corresponds to the material properties of the base material, and χ^{kl} are a set of periodic functions resulting from the solution to a problem of six equilibrium equations, defined on the micro cell domain.

3.2 Optimization problem

The bone remodelling model assumes that bone adapts to the mechanical environment to obtain the stiffest structure for the applied loads to which it is subjected. Mathematically, the process of bone adaptation is defined as the minimization of the structural compliance, thus maximizing the structural stiffness, while taking into account the metabolic cost associated with bone tissue maintenance. Bone is considered as a structure occupying a volume Ω with boundary Γ, subjected to a set of surface loads $\boldsymbol{t}^P$ and the corresponding displacements field $\boldsymbol{u}^P$. Considering the parameters $\boldsymbol{a}$ and $\boldsymbol{\theta}$ of the local microstructures design variables, the optimization problem can be stated as

$$min\left\{\sum_{P=1}^{NC}\alpha^P\left(\int_\Gamma t_i^P\, u_i^P\, d\Gamma\right) + k\int_\Omega \rho(\boldsymbol{a})^m\, d\Omega\right\}, \qquad (3\text{-}3)$$

subjected to

$$0 \leq a_i \leq 1\ , i = 1,2,3$$
$$\int_{\Omega} E^H_{ijkl}(\boldsymbol{a}, \boldsymbol{\theta})\, \varepsilon_{ij}(\boldsymbol{u}^P)\varepsilon_{kl}(\boldsymbol{v}^P) d\Omega = \int_{\Gamma} t_i^P\, u_i^P\, d\Gamma, \tag{3-4}$$

where NC is the number of applied loads and α^P are the load weight factors satisfying $\sum_{P=1}^{NC} \alpha^P = 1$. Equation 3-3 represents the objective function. The first term is a weighted average of the structural compliance for each load case, whereas the second term is related to the metabolic cost of bone tissue maintenance. It is well known that bone adaptation differs among individuals, even in the presence of equal loading cases. This is related to several biological factors such as age, hormone status, disease, and so on. In the second term of equation 3-3, the parameters k and m allow the adjustment of the model to different biological situations. Both of them play an important role in the bone remodelling model, since the optimal bone mass will rely heavily on their value (Quental, 2013). The parameter k represents the metabolic cost per unit of bone volume. Accordingly, an increase in k is associated with a bone structure that presents lower bone mass, since the bone homeostasis maintenance cost to the organism is higher. The parameter m represents a corrective factor for the preservation of intermediate densities. Hence, an increase in m corresponds to an increase of the intermediate density regions, mitigating the formation of regions with extreme densities (Quental, Folgado, et al., 2014). Equation 3-4 corresponds to the set of equilibrium equations, in the form of a virtual displacement principle. In this equation, ε_{ij} and ε_{kl} correspond to the components of the strain field and $\boldsymbol{v}^P$ to the set of virtual displacements.

The optimization problem (equations 3-3 and 3-4) is solved through a Lagrangian method, described in detail in Folgado et al. (2004). The stationary conditions related to the design variables $\boldsymbol{a}$ and $\boldsymbol{\theta}$ are formulated by

$$\sum_{P=1}^{NC} \left[-\alpha^P \int_{\Omega} \frac{\partial E^H_{ijkl}(\boldsymbol{a}, \boldsymbol{\theta})}{\partial \boldsymbol{a}} \varepsilon_{ij}(\boldsymbol{u}^P)\varepsilon_{kl}(\boldsymbol{v}^P)\, d\Omega \right] + k \int_{\Omega} m\rho^{m-1} \frac{\partial \rho}{\partial \boldsymbol{a}} = 0 \tag{3-5}$$

and

$$\sum_{P=1}^{NC} \left[-\alpha^P \int_{\Omega} \frac{\partial E^H_{ijkl}(\boldsymbol{a}, \boldsymbol{\theta})}{\partial \boldsymbol{\theta}} \varepsilon_{ij}(\boldsymbol{u}^P)\varepsilon_{kl}(\boldsymbol{v}^P)\, d\Omega \right] = 0, \tag{3-6}$$

where the displacement field $\boldsymbol{u}^P$ and the adjoint field $\boldsymbol{v}^P$ are obtained from the stationary conditions with respect to $\boldsymbol{v}$ and $\boldsymbol{u}$, respectively. Equations 3-5 and 3-6 express the law of bone remodelling. When both equations are satisfied, the process of bone adaptation is stabilized (P. Fernandes et al., 1999; Quental, 2013).

Generally, the remodelling equations are solved numerically with the finite element method, based on the element-based approach, which considers that each element has a uniform density. In this work, a node-based approach was used instead. In this approach, the design variables are defined at the nodes, rather than at the element centroids (Jacobs et al., 1995). The homogenised properties and densities at each integration point result from the interpolation of the design variables at the nodes to the integration points

of each element (Quental, 2013). The numerical equations used to describe the node-based approach can be found in Quental (2013).

3.3 Numerical simulation

The computational model, illustrated in Figure 3-2, is built as an iterative process that continuously updates the mechanical properties of bone until the optimal conditions are met. Initially, the homogenized elastic properties are computed for an initial solution. Then, the displacement field is computed using the finite element method in ABAQUS®. Subsequently, the optimal conditions are verified. If they are satisfied, i.e., if the bone adaptation process is considered stabilized, the process stops, otherwise the process restarts with updated values of the design variables. At each k_{th} iteration the design variables are updated as

$$(\boldsymbol{a})_{k+1} = \begin{cases} \max[(1-\zeta)(\boldsymbol{a})_k, \boldsymbol{a}_{min}], if\ (\boldsymbol{a})_k + s(\boldsymbol{D}_a)_k \leq \max[(1-\zeta)(\boldsymbol{a})_k, \boldsymbol{a}_{min}] \\ (\boldsymbol{a})_k + s(\boldsymbol{D}_a)_k, \qquad otherwise \\ \min[(1+\zeta)(\boldsymbol{a})_k, \boldsymbol{a}_{max}], if\ (\boldsymbol{a})_k + s(\boldsymbol{D}_a)_k \geq \min[(1+\zeta)(\boldsymbol{a})_k, \boldsymbol{a}_{max}] \end{cases} \tag{3-7}$$

$$(\boldsymbol{\theta})_{k+1} = (\boldsymbol{\theta})_k + s(\boldsymbol{D}_\theta)_k$$

where $\boldsymbol{a}_{min}$ and $\boldsymbol{a}_{max}$ correspond to the minimum and maximum boundaries of $\boldsymbol{a}$, respectively; s is the step length of the optimization defined by the user; $\boldsymbol{D}_a$ and $\boldsymbol{D}_\theta$ are the descent directions of $\boldsymbol{a}$ and $\boldsymbol{\theta}$, respectively; and ζ defines the upper and lower bound contraints in density related with equations 3-5 and 3-6, thus preventing large transitions of density among iterations.

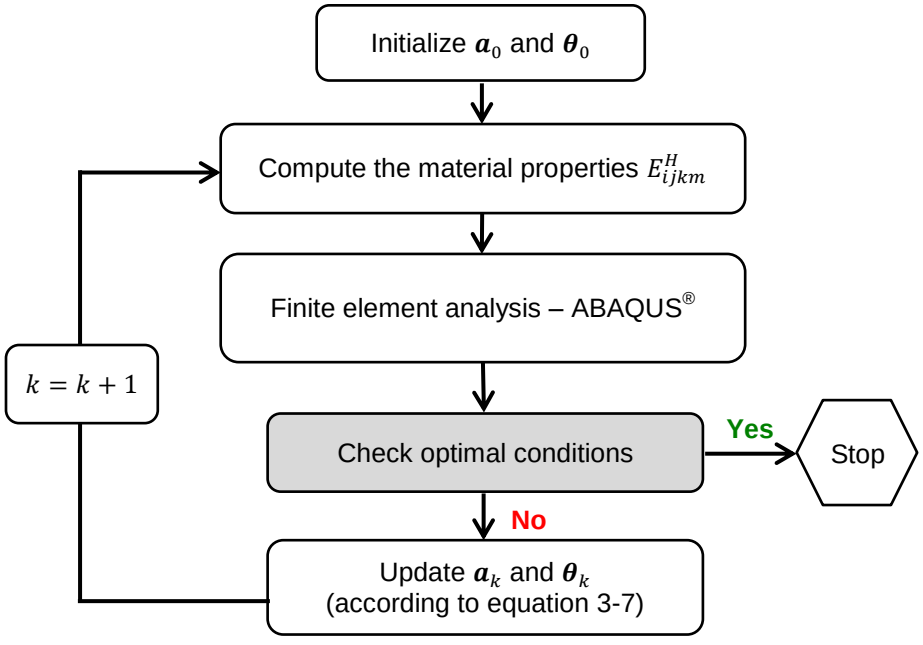

Figure 3-2 Flowchart of the bone remodeling computational model (Adapted from Chan (2014) and P. R. Fernandes et al. (2002))

Chapter 4

Computational modelling

In this chapter, the geometric modelling of the bone and implants, finite element modelling, bone remodelling modelling and methodology for the analysis of the results are described in detail.

4.1 Geometric model

In this section the detailed phases followed to develop the three-dimensional solid models of the intact bone and the shoulder prostheses are described.

4.1.1 Intact bone

The 3D anatomical model of the proximal right humerus was generated using a geometric modelling sequence that receives as input a stack of computed tomography (CT) medical images and returns as output the 3D geometric model. A finite element model of the created solid model was then generated. The geometric modelling sequence includes several steps, such as: image acquisition, image segmentation, surface mesh adjustments and solid model generation (Ribeiro et al., 2009). All of these steps are further described with the exception of the image acquisition process, since the CT images used were obtained from the Visible Human Project, VHP (Spitzer et al., 1996).

In order to decrease the computational cost, and since the changes in bone adaptation due to the insertion of an implant occur mainly in its adjacent areas, only the proximal humerus was modelled.

4.1.1.1 Image segmentation

Image segmentation is the process of partition of a digital image into non-overlapping regions, in which each region is the position of an object. These regions are homogeneous with respect to specific image features such as intensity or texture, facilitating the delimitation of particular regions of interest. Segmentation plays an essential role in anatomical modelling by establishing the conversion of medical image data into 3D mesh data (Pham et al., 2000; Ribeiro et al., 2009).

The software used in this process was ITK-SNAP (version 3.4.0, 2015), an open source freeware (Yushkevich et al., 2006). Besides the manual delineation and image navigation, it offers semi-automatic

segmentation employing active contours methods. Three methods were combined to deal with the bone segmentation problem: global thresholding, active contour method and manual segmentation.

Before setting the parameters of global thresholding, it was necessary to adjust image contrast and specify the region of interest, to better identify the right humerus' boundaries in CT images.

In CT images, the pixels' intensity of the object of interest lies between two user-defined values. Thresholding resides on selecting the intensities that detect the tissue of interest – image foreground – excluding the other intensities – image background – thus, approximating the location of the desirable tissue. After the image has been filtered by the threshold, the original intensity values are mapped into new ones, ranging from -1 to 1, where the background and foreground pixels correspond to the lower and upper extremities, respectively. Pixels with values near zero indicate a limit between the required and non-required anatomical structure (Ribeiro et al., 2009).

The active contour method is a semi-automatic approach based on deformable models such as spherical bubbles. These bubbles present physical properties that, under the stimulus of internal and external mechanical forces, deform according to image contours and delineate boundaries for the different regions of the anatomical structure of interest. The deformation evolves as an iterative process. Based on the probability of a voxel belonging to the structure of interest or to the background, internal and external forces of every voxels are computed for each iteration T. These probabilities are estimated based on the threshold function. When the deformable surfaces enclosure every voxel with considerable probability value or the user finds a proper result, the process ends (Ribeiro et al., 2009). The evolution of the active contour method along different iterations is presented in Figure 4-1. Iteration T=0 shows the contour initialization as a rough estimate of the right humerus, whereas iteration T=250 represents a great approximation of it although with an extended region identified outside of the humerus in the inferior boundary of the coronal section, as depicted in Figure 4-1 (c).

The outcome of the active contour method is not absolutely accurate since segmentation errors may occur (Ribeiro et al., 2009). Therefore, corrections have to be performed using manual segmentation.

4.1.1.2 Surface mesh adjustments

At the end of the image segmentation step, a 3D surface was created. The surface presented undesirable features such as stair-step shape effects and excess of nodes and facets, as illustrated in Figure 4-2 (a). To improve the surface mesh, the open source freeware, Meshlab (version 1.3.3, 2014) was used (Cignoni et al., 2008). The surface model of the humerus was smoothed by a low-pass filter, known as Laplacian smoothing filter, whose outcome is shown in Figure 4-2 (b). This filter is used to amend the step-like artefacts produced during segmentation, polishing up the surface mesh appearance (Ribeiro et al., 2009). Besides that, the duplicated nodes and facets were removed and specific sharp edges were corrected using a manual tool, as illustrated in Figure 4-2 (c). The model was exported from Meshlab as a point cloud data file.

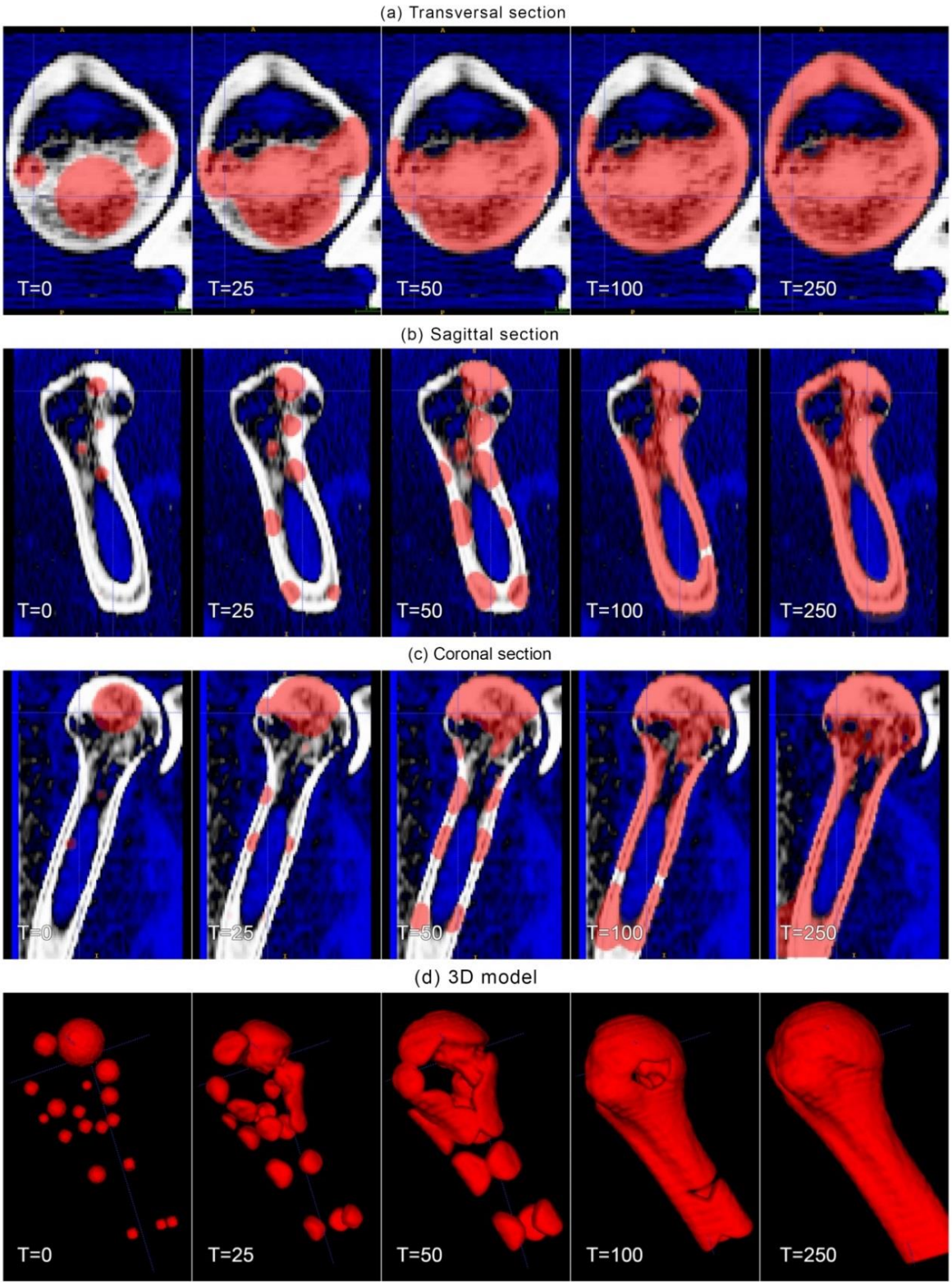

Figure 4-1 Evolution of the active contour method along different iterations (T=0, T=25, T=0, T=50, T=100 and T=250). (a) Transversal section. (b) Sagittal section. (c) Coronal section. (D) 3D model.

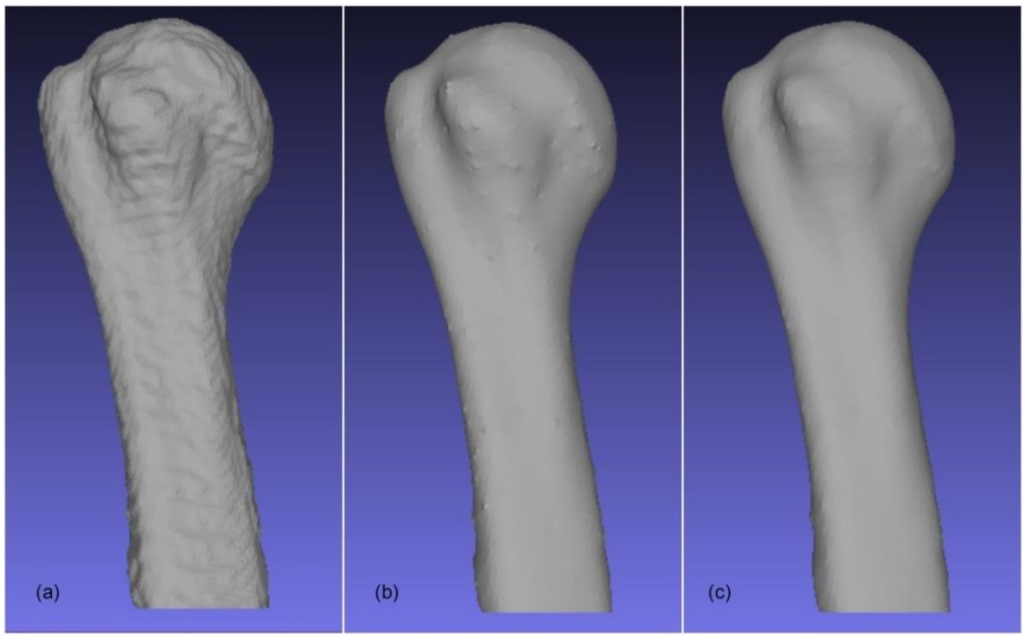

Figure 4-2 Adjustments on the surface mesh of the right humerus (Anterior view). (a) 3D surface model obtained in the segmentation step. (b) Smoothed model. (c) Model obtained in the end of the surface mesh adjustment step.

4.1.1.3 Solid model generation

In this step the surface mesh was converted into a solid model using the ScanTo3D® tool of the commercial software Solidworks® (version SP02.1, 2015). This tool automatically creates solid models from mesh or point cloud data, which are subsequently imported to a finite element software for tetrahedral or hexahedral volume mesh generation (Ribeiro et al., 2009). The 3D model obtained for the proximal humerus is presented in Figure 4-3. The feature lines observed on the humerus define the boundaries between different superficial mesh elements automatically generated in Solidworks®.

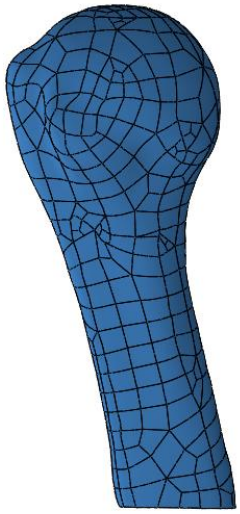

Figure 4-3 Anterior view of the solid model of the right proximal humerus generated from the surface mesh in Figure 4-2 (c).

4.1.2 Implants

After the development of the intact bone model, the solid models of a resurfacing implant and a stemless implant were developed based on the Global C.A.P.™ Resurfacing Humeral Head Implant from DePuy and on the Sidus™ Stem-Free Shoulder from Zimmer, respectively. Henceforth, the modelled implants will be simply referred to as Global CAP and Sidus. The implants can be used either in hemi or total shoulder arthroplasty and are only indicated for uncemented techniques (DePuy, 2004; Zimmer, 2012). The models were created in Solidworks®.

Since there is a significant variability in humeral head size anatomy among individuals, both implants are available in several head heights that correlate with specific head diameters, in order to provide the best possible replacement. Thus, to understand which head implant size would be most suitable to the humeral head modelled, the following relation was used, according to Klawitter et al. (2014):

$$R = \frac{D^2 + 4H^2}{8H} \tag{4-1}$$

where H is the height, D is the diameter and R is the radius of the humeral head. The radius and the centre of the head were obtained using a Matlab® (version R2014a, 2014) function that fits a sphere to the humeral head using a set of 3D data points. Figure 4-4 schematizes the relationship between the variables in equation 4-1.

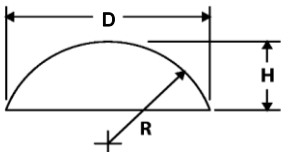

Figure 4-4 Circular segment of a sphere's cap

4.1.2.1 Global CAP

The Global CAP is a resurfacing humeral head implant composed of a single component with a cruciate stem that improves implant rotational stability. The Global CAP options present variable stem lengths for corresponding head heights. The available sizes conjugating the different combinations of head heights and diameters are presented in Table 4-1. The stem lengths are 30 mm, 35 mm and 40 mm for head heights of 15 mm, 18 mm and 21 mm, respectively.

Table 4-1 Variable sizing options for the Global CAP (DePuy, 2004)

Anatomic sizing		Head diameters (mm)				
		40	44	48	52	56
Head heights (mm)	15	X	X			
	18	X	X	X	X	X
	21			X	X	X

Since it was not possible to obtain a real model of the implant to measure its effective proportions, a scheme of the cross-section of the Global C.A.P.^{TM} implant (DePuy, 2004) was used as a starting point to model the implant. This scheme is presented in Figure 4-5, together with the cross-section of the solid model of the implant with the considered dimensions.

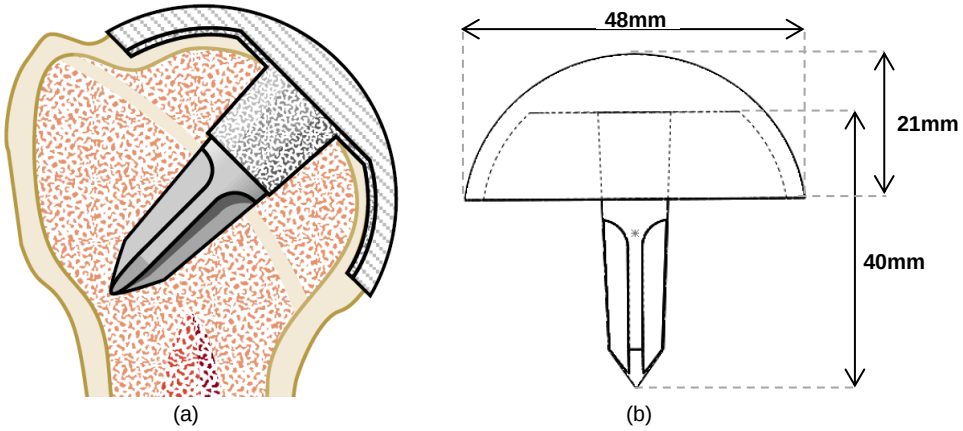

Figure 4-5 Cross-section of the Global CAP implant. The Global C.A.P.^{TM} implant from DePuy (DePuy, 2004) and the modelled implant with the considered dimensions are represented in (a) and (b), respectively.

The Global C.A.P.^{TM} Resurfacing Humeral Head implant from DePuy and the final solid model are illustrated in Figure 4-6.

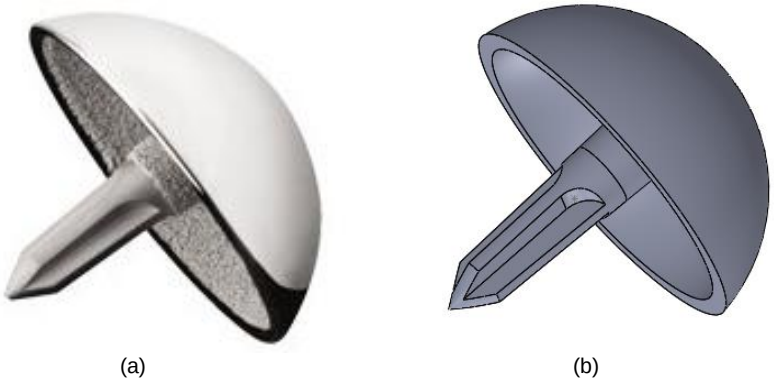

Figure 4-6 Illustration of the Global C.A.P.^{TM} Resurfacing Humeral Head implant from DePuy (DePuy, 2004), in (a), and the final solid model of the Global CAP, in (b).

4.1.2.2 Sidus

The sidus is a humeral head stemless implant composed of two distinct components: the humeral head and the humeral anchor. They are fitted together by a taper connection. The anchor is composed of 4 perpendicular rough blasted anchorage fins. Table 4-2 shows the available range of humeral heads, with the different heights and diameters, as well as the range of humeral anchors.

Table 4-2 Variable sizing options of Sidus (Zimmer, 2012)

Head	Diameter	38	40	42	44	44	46	48	50	52
	Height	13	14	15	16	16	16	17/20	18/21	19/23
Anchor		S				M			L	

The sizes S, M and L of the humeral anchor correspond to 24 mm, 28 mm and 32 mm in diameter D, and 16 mm, 19 mm and 22 mm in height H, respectively. The implant was designed based on the schemes of Figure 4-7 (a). The cross-section of the modelled humeral head and anchor are presented in Figure 4-7 (b) with the considered dimensions.

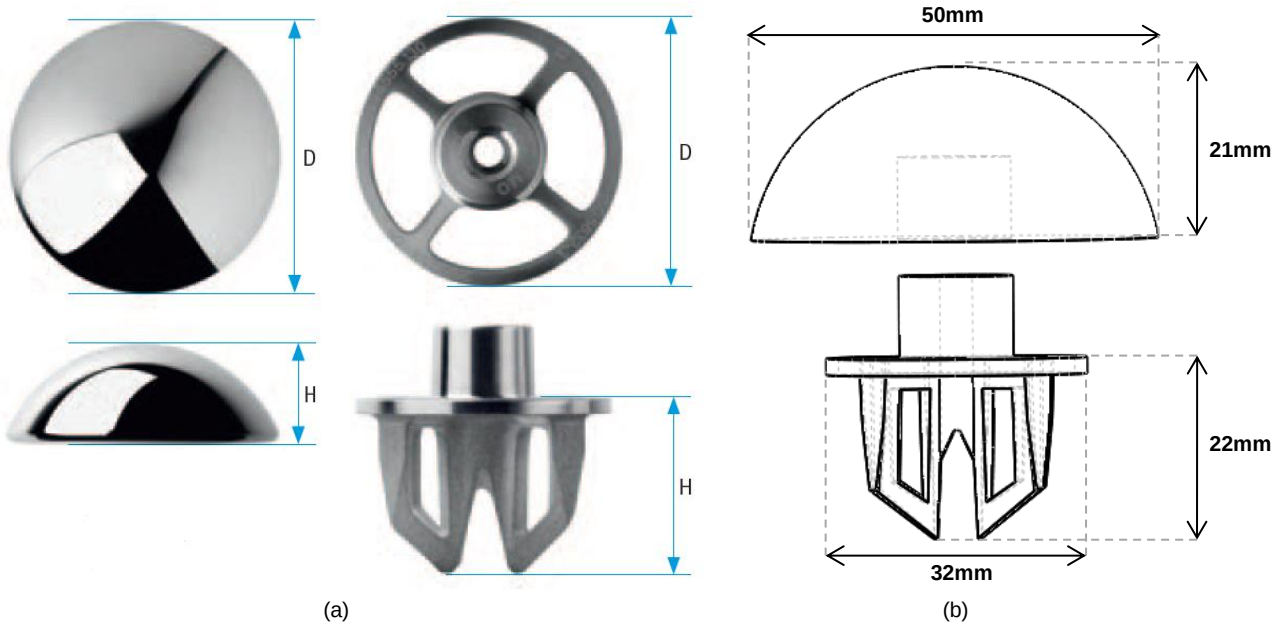

Figure 4-7 Superior and frontal view of the Sidus™ Stem-Free Shoulder humeral head and anchor (Zimmer, 2012) in (a), and cross-section of the modelled humeral head and anchor with the considered dimensions in (b).

The Sidus™ Stem-Free Shoulder implant from Zimmer and the final solid model are illustrated in Figure 4-8.

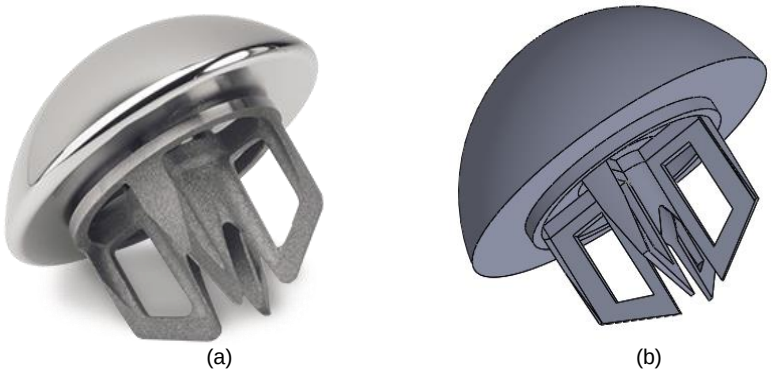

Figure 4-8 Illustration of the Sidus™ Stem-Free Shoulder implant from Zimmer (Zimmer, 2012), in (a), and the final solid model of Sidus, in (b).

4.1.3 Assembly – Intact bone and implants

The shoulder arthroplasty was virtually simulated in Solidworks® for the two implants described. The implant positioning was approved by an orthopaedic surgeon.

4.1.3.1 Global CAP implantation

To ensure the correct placement of the Global CAP implant on the humerus it is important to understand its surgical procedure. Accordingly, a brief overview is provided here. After the osteophyte removal, the head size is verified intraoperatively using the humeral head sizers or humeral head gauge. The appropriate head sizer is determined by identifying the articular margin of the humerus in relation to the inferior edge of the sizer. If the articular margin is 3 mm below the inferior edge of the sizer, a deeper head height is necessary as illustrated in Figure 4-9 (a). Then, the appropriate humeral head sizer is assembled to the drill guide handle and the necessary measurements are taken to identify the centre of the humeral head. Based on previously determined head size, the humeral head is shaped with the appropriate size reamer, as depicted in Figure 4-9 (b); a trial implant is used to assess the proper size and fit; and a cruciform stem punch is used to create a path for the implant stem into the cancellous bone of the humerus. After appropriate soft-tissue releasing to maximise postoperative range of motion, the implant is finally placed as shown in Figure 4-9 (c). A detailed description of the surgical technique can be found in DePuy (2004).

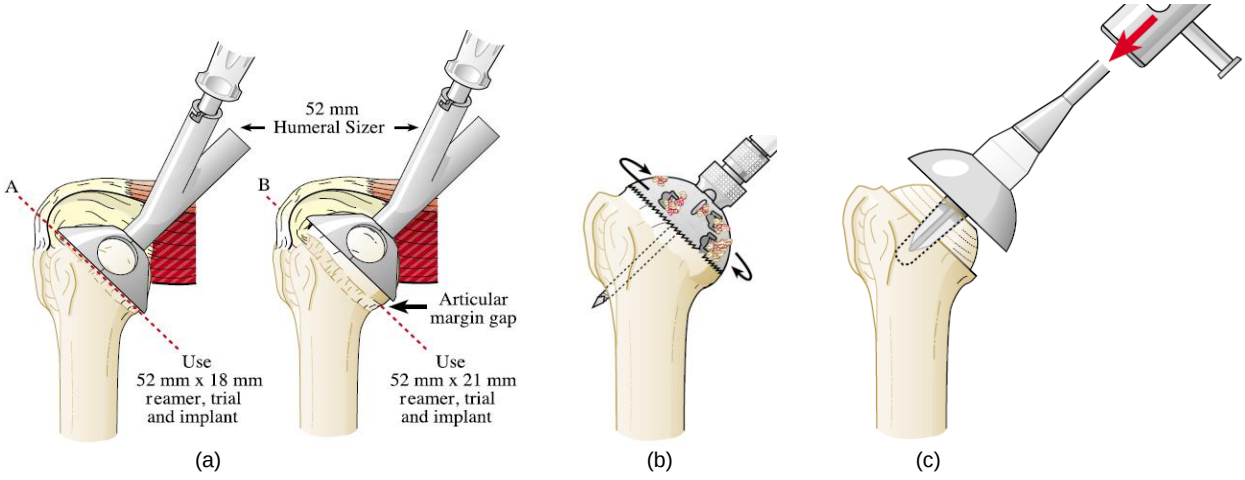

Figure 4-9 Surgical procedure of the resurfacing shoulder arthroplasty with the Global CAP implant. (a) Head sizing assessment. (b) Humeral head shaping with the appropriate size reamer. (c) Implant placement with the head impactor tool. (DePuy, 2004)

In order to assemble the Global CAP into the intact bone with the correct alignment, it was necessary to define a plane parallel to the articular margin gap to make its perpendicular axis – the axis of the humeral head – and the axis of the implant's stem coincident. After some iterations, the optimal combination between the head diameter and height was reached as shown in Figure 4-10 (a). Then, the bone was cut into the shape that matches the corresponding surface of the Global CAP implant, using cutting tools of Abaqus®, as depicted in Figures 4-10 (b) and (c).

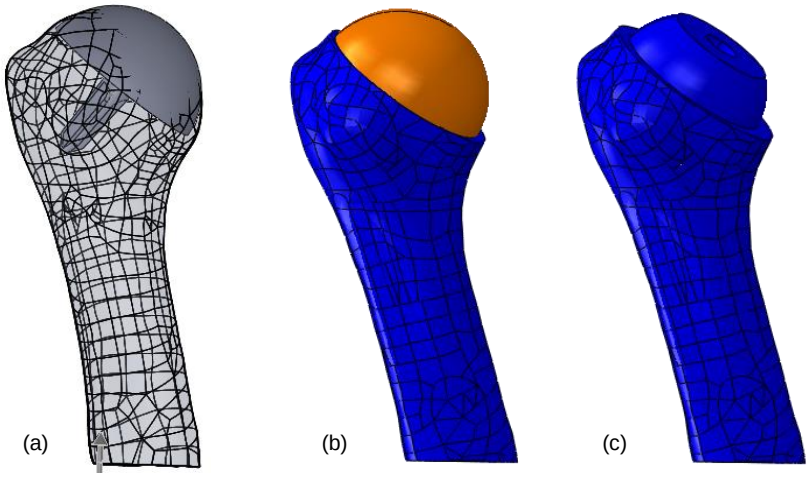

Figure 4-10 Anterior view of the humerus after the implantation of the global CAP implant: (a) Solidworks® positioning. (b) After the cut in Abaqus®, with the implant. (c) After the cut in Abaqus®, without the implant.

4.1.3.2 Sidus implantation

To understand the best way to place the Sidus implant on the humerus, a summarized overview of the surgical procedure is provided. After the osteophyte removal, the humeral head is resected at the level of the anatomical neck, as shown in Figure 4-11 (a). The trial head size that covers the resected humeral osteotomy is determined and positioned with a central pin. Then, the size of the anchor is determined by using the anchor sizer. The inner open ring should cover most of the cancellous bone, without involving the cortex and the outer ring should be centric to the resected humeral surface, as illustrated in Figure 4-11 (b). With the appropriate anchor sizer and the countersink, the surface is drilled. After the humerus puncher is impacted over the central pin, it is removed and the humerus is finally prepared for the implantation of the humeral anchor, as depicted in Figure 4-11 (c). Thereafter, the definitive humeral head is placed, sitting flush on the osteotomy plane, as shown in Figure 4-11 (d). For a more detailed explanation of the surgical procedure, see Zimmer (2012).

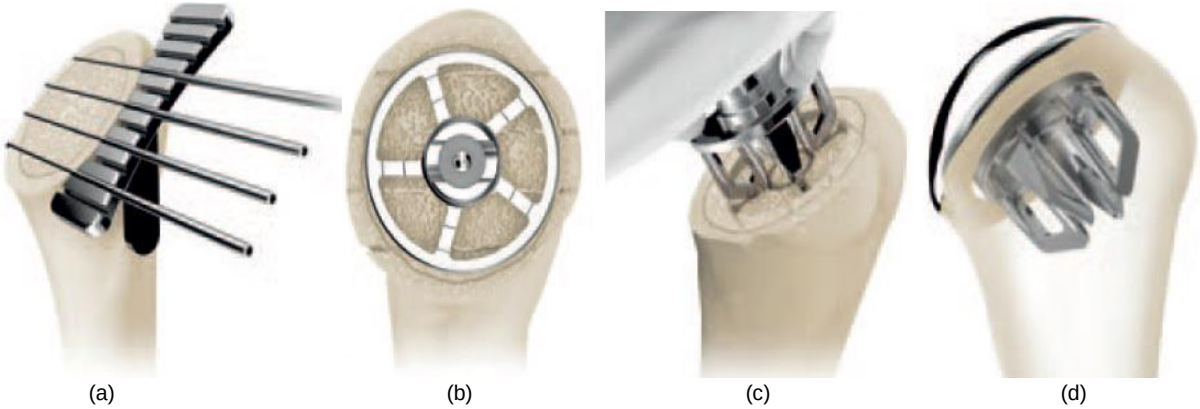

Figure 4-11 Surgical procedure of the stemless shoulder arthroplasty with the Sidus implant. (a) Resection of the humeral head (b) Humeral anchor sizing assessment. (c) Humeral anchor implantation. (d) Head and anchor implanted. (Zimmer, 2012)

The assembly of the Sidus implant into the intact bone was similar to the assembly of the Global CAP implant. A parallel plane to the anatomical neck was also defined to make its perpendicular axis – the axis of the humeral head – coincident with the axis of the implant's stem. However, taking into account the indications of the surgical procedure, the cutting plane was placed about 2.5 mm away from the proximal end of humerus, compared to the Global CAP implant. The optimal combination between head diameter and height is shown in Figure 4-12 (a). Note that the diameter and the height of the head of the implants are different among the implants modelled, since the available options provided by the manufacturers are distinct. Using cutting tools of Abaqus®, the bone was cut into the shape that matches the corresponding surface of Sidus implant, as represented in Figures 4-12 (b) and (c).

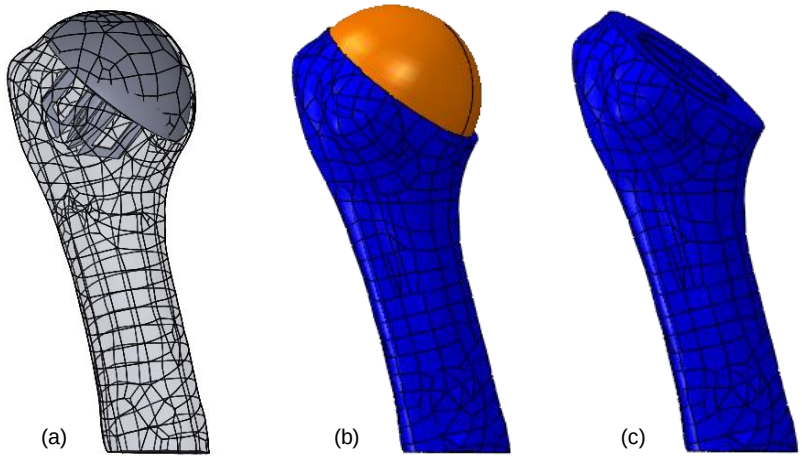

Figure 4-12 Anterior view of the humerus after the implantation of the Sidus implant: (a) Solidworks® positioning. (b) After the cut in Abaqus®, with the implant. (c) After the cut in Abaqus®, without the implant.

4.2 Finite element model

The finite element method (FEM) is a powerful numerical method used to approximate the solutions of mathematical problems that simulate the behaviour of complex physical systems. The largest problem is solved by its subdivision into smaller and simple problems composed of finite elements. The set of all finite elements comprise the finite element mesh. The elements are connected with each other through points, commonly known as nodes. The equations that model each finite element are then assembled into a greater system of equations to obtain the solution to the whole problem (Reddy, 2006). The finite element model, created in the commercial software Abaqus® (version 6.14-5, 2014), is described in this section.

4.2.1 Material properties and interfaces interaction

Bone was modelled as a linear elastic cellular material with an orthotropic microstructure. The relative density distribution of bone results from the solution of the optimization problem that integrates the finite element method with a numerical simulation of the process of bone adaptation. A maximum Young's modulus of $18\ GPa$ and a Poisson's ratio of 0.3 were considered for bone (Gupta & Dan, 2004; Quental et al., 2012; Quental, Folgado, et al., 2014).

The head of both implants is made of a Cobalt-Chromium alloy (CoCrMo), while the stem in the Global CAP and the anchor in Sidus are made of a titanium alloy ($TiAl_6V_4$). All of the implants structures were considered homogeneous, isotropic and linear elastic. The material properties considered are summarized in Table 4-3 (Quental et al., 2012).

Table 4-3 Material properties of the implant components.

Material	Young's modulus (E, GPa)	Poisson's ratio(ν)
Cobalt-chromium alloy	230	0.3
Titanium alloy	115	0.3

The interaction between the bone and the implants was defined according to the different properties of the implants. In the Global CAP, the undersurface of the head and the proximal portion of the stem are covered with a porous or a hydroxyapatite (HA) coating, which promotes bone ingrowth (DePuy, 2004). In the Sidus, the anchor is composed of a rough surface that promotes long lasting osseointegration (Zimmer, 2012). Considering an idealized condition of full osteointegration, the interaction between these surface regions of the implant and the corresponding bone surface was considered rigidly bonded with a tie constraint (Dassault, 2012). The interface between the head and anchor in Sidus was also considered bonded. Contact was defined between the distal stem of the Global CAP and the bone, and between the bone and the rim of the Sidus' implant in contact with bone, considering friction coefficients of 0.36 (Eberle & Augat, 2007) and 0.26 (Sobocinski, 2015), respectively. A penalty friction formulation was considered to model the frictional interaction. At last, the interaction between bone and the non-coated rim of the Global CAP was defined in two different ways: with contact, for a coefficient of friction of 0.26, and without contact. A scheme of the interactions implant-bone is illustrated in Figure 4-13.

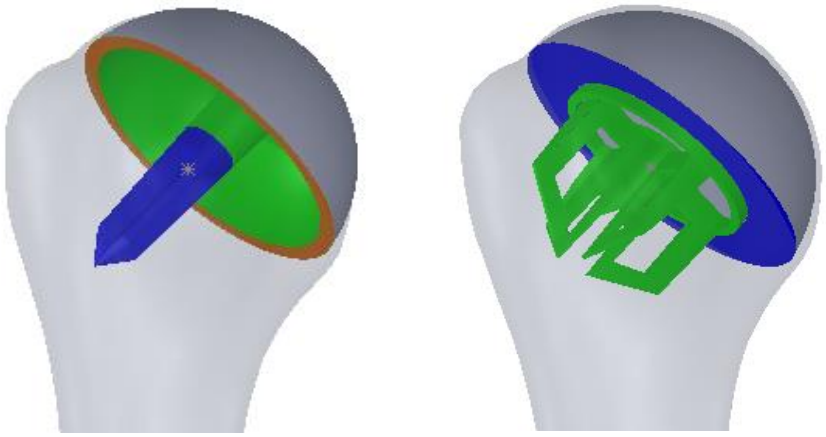

(a) (b)

Figure 4-13 Anterior view of the interactions implant – bone for the Global CAP, in (a), and for the Sidus, in (b). The surfaces depicted in green represent a bonded contact (tie constraint), in blue represent a frictional contact and in orange represent either an absence of contact or frictional contact.

4.2.2 Loading and boundary conditions

In order to properly characterize the mechanical environment of bone, several important muscle loads responsible for the appropriate functioning of the humerus within the shoulder complex were considered, including the Supraspinatus, Subscapularis, Pectoralis Major, Latissimus Dorsi, Teres Major, Deltoid, Coracobrachialis, Infraspinatus, Teres Minor, Biceps brachii and Triceps brachii muscles. The insertion, origin and action of these muscles is described in Chapter 2, section 2.3.3.

Six different load cases were applied to the model. These include muscle and joint reaction forces at 10º, 60º and 110º of arm abduction in the frontal plane and anterior flexion in the sagittal plane. The data regarding the magnitude of muscle and glenohumeral joint reaction forces was acquired using the multibody musculoskeletal model of the upper limb developed by Quental (2013). The model used in this work and the model from Quental (2013) are based on the same subject and thus, identical. However, since the global coordinate systems of the two models are different, it was necessary to transform the forces from the global coordinate system of the model of Quental (2013) to the global coordinate system of the model described in this work. To accomplish that, an Iterative Closest Point algorithm in Matlab® was used. This algorithm receives as input the point clouds of the humerus from both models and returns the rigid transformation, i.e., the rotation matrix R and translation vector T, that best align the two point clouds. The muscle and joint reaction forces applied to the humerus are presented in Table 4-4.

The muscle forces were applied on attachment points located in the centroid of each muscle site, which was defined directly on the bone surface according to Netter (2006), as illustrated in Figure 4-14. The attachment points are independent of the mesh, being able to transfer force to the model through the definition of *coupling* constraints. With respect to the muscle forces, these constrains connect the attachment points to the corresponding nodes of the muscle sites at the bone surface, as shown in Figure 4-14.

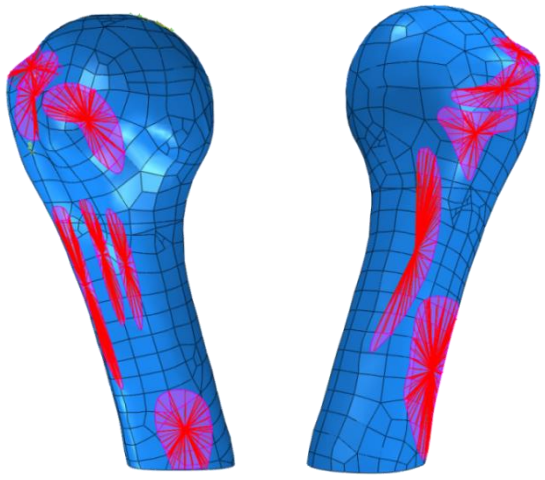

Figure 4-14 Muscle sites where the six load cases were applied. The coupling interactions are also illustrated. On the left side the muscles presented are: Supraspinatus, Subscapularis, Pectoralis Major, Latissimus Dorsi, Teres Major, Biceps brachii and Coracobrachialis (Anterior view). On the right side the muscles presented are: Supraspinatus, Infraspinatus, Teres Minor, Deltoid and Triceps brachii (Posterior view).

Regarding the glenohumeral joint reaction forces, they were also applied in attachment points; however, instead of defining the connected nodes in Abaqus®, an algorithm was developed in Matlab® to select all the surface humeral head nodes within a circular region centred at the force application point. The force applied at the attachment point was distributed by the coupling nodes through a uniform and quadratic weighting methods for the muscle and glenohumeral joint forces, respectively. In the uniform weighting method the same force is applied to all nodes, while in the quadratic weighting method the force decreases with radial distance from the attachment point (Dassault, 2012).

Table 4-4 Muscle and joint reaction forces, in *N*, for the six load conditions at 10º, 60º and 110º of arm abduction and anterior flexion. The forces are in the global coordinate system of the right humerus described in this work.

		Abduction			Flexion		
Muscle	**Direction**	**10º**	**60º**	**110º**	**10º**	**60º**	**110º**
Pectoralis major	X	-6.872	-0.000	-8.946	-11.708	-0.000	0.020
	Y	3.964	0.000	-2.689	3.314	-0.000	-0.526
	Z	6.209	0.000	4.267	8.259	0.000	0.208
Latissimus dorsi	X	0.000	-0.000	-0.000	-0.000	-0.000	-0.000
	Y	-0.000	-0.000	-0.000	-0.000	-0.000	-0.000
	Z	-0.000	0.000	0.000	-0.000	0.000	0.000
Deltoid	X	-3.247	-21.133	-16.293	-3.944	-116.803	-94.034
	Y	4.411	43.141	41.836	5.579	67.494	44.453
	Z	33.353	153.151	140.902	12.522	183.417	134.180
Subscapularis	X	-0.000	-0.000	-0.000	-0.000	-2.319	5.653
	Y	-0.000	-0.001	-0.000	-0.001	-42.257	-26.881
	Z	-0.000	0.000	0.001	0.000	63.736	120.498
Supraspinatus	X	-2.679	-6.556	10.254	-14.204	-7.119	-0.000
	Y	-20.629	-59.850	-9.962	-44.916	-12.033	-0.000
	Z	26.678	86.470	96.641	59.127	19.709	0.000
Infraspinatus	X	2.533	-3.868	-14.801	10.415	19.918	2.308
	Y	-22.625	-107.316	-79.902	-56.406	-94.582	-6.298
	Z	9.068	67.401	97.566	19.342	73.190	15.129
Teres major	X	0.000	-0.000	-0.000	0.000	0.000	0.000
	Y	-0.000	-0.000	-0.000	-0.000	-0.000	-0.000
	Z	-0.000	0.000	0.000	0.000	0.000	0.000
Teres minor	X	-0.000	0.000	-0.383	0.000	3.059	3.547
	Y	-0.000	-0.000	-9.294	-0.000	-11.406	-24.355
	Z	-0.000	0.000	8.522	-0.000	7.568	53.839
Coracobrachialis	X	-0.000	-0.000	-0.000	-0.000	-0.000	-0.000
	Y	0.000	0.000	0.000	0.000	0.000	0.000
	Z	0.000	0.000	0.000	0.000	0.000	0.000
Biceps brachii	X	15.793	20.775	0.000	46.323	0.000	0.000
	Y	-5.181	-23.930	-0.000	-19.326	-0.000	-0.000
	Z	-4.637	-14.961	-0.000	-12.926	-0.000	-0.000
Triceps brachii	X	0.000	0.000	11.654	0.000	0.000	10.759
	Y	-0.000	-0.000	-4.934	-0.000	-0.000	-4.555
	Z	-0.000	-0.000	-14.643	-0.000	-0.000	-13.519
Glenohumeral joint	X	17.022	61.432	55.091	12.562	49.841	28.533
	Y	65.764	200.585	93.007	174.982	185.282	52.792
	Z	-11.299	-277.410	-362.112	-36.295	-381.190	-342.590

The lower extremity of the humerus was fixed by an *encastre* condition, which constrains all displacements and rotations (Dassault, 2012).

4.2.3 Mesh generation

Two types of elements are commonly used to generate the three-dimensional mesh: tetrahedral and hexahedral. Usually, hexahedral elements are preferred because they lead to better results regarding convergence rate and accuracy of the solution. However, due to the complex geometry of the structures being modelled, a tetrahedral mesh was chosen instead (Tadepalli et al., 2011). Linear elements (four-noded elements) were selected over quadratic elements (ten-noded elements) due to inherent limitations of the bone remodelling model used in this work. Thus, linear tetrahedral elements (C3D4 elements) were used to mesh all the parts of the models, i.e., the intact bone, the implanted bone and the Global CAP and Sidus implants.

A convergence analysis was conducted to select the best mesh refinement for the intact bone. Thus, by comparing the Von Mises stress and the time of the analysis for each refined mesh, an optimal mesh refinement solution of 2 mm was selected. The mesh convergence analysis is presented in Figure 4-15.

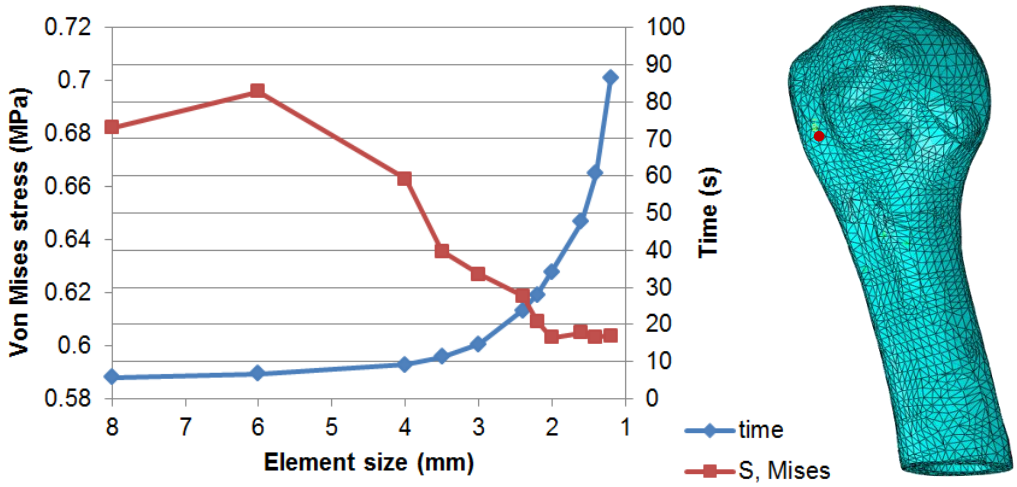

Figure 4-15 Mesh convergence analysis to select the best element size for the finite element mesh of the intact bone. Both Von Mises stress and time for each mesh refinement analysis were considered. The red dot in the FEM of the intact bone represents the reference point considered to perform the mesh convergence analysis.

Considering the design of the implants, differences in the bone remodelling process are likely to occur near the humeral head. Given that, for the implanted bone, a smaller element average length of 1.5 mm was imposed on the humeral head. In order to avoid increasing the computational cost of the simulations, an element average length of 3 mm was used for the humeral distal section. All the components of the implants were meshed with an element average length of 2 mm. Figure 4-16 presents the finite element meshes generated for the intact and implanted bones and for the different implants modelled.

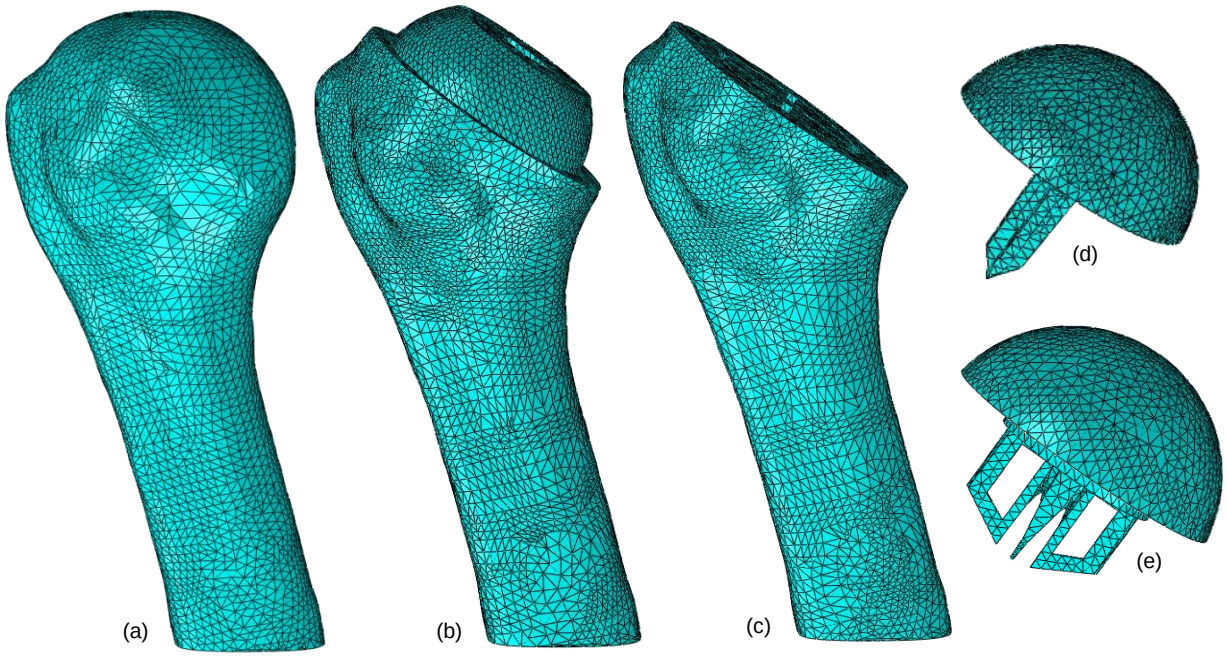

Figure 4-16 Anterior view of the finite element meshes. (a) Intact bone; Implanted bone with the (b) Global CAP implant and the (c) Sidus implant; (d) Global CAP implant; (e) Sidus implant.

A description of the resulting meshes is provided in Table 4-5, regarding the number of elements and nodes.

Table 4-5 Description of the finite element meshes generated.

Model			Elements	Nodes
Intact bone			98971	19685
Assembly	Implanted bone		150339	29188
	Global CAP implant		14585	3562
Assembly	Implanted bone		130907	25795
	Sidus implant	head	24636	4988
		anchor	4423	1499

4.3 Bone remodelling model

The load weight factors α^P, described in equation 3-3, were defined according to the relative frequencies of each movement (abduction and flexion) and arm positions during daily activities. For the arm elevations of 10º, 60º and 110º, they were 0.231504, 0.077910, 0.008586 for abduction and 0.496496, 0.167090, 0.018414 for flexion, respectively (Coley et al., 2008, 2009). The simulations were performed following a node-based approach and with a step length s of 10.

4.3.1 Validation of the bone remodelling model for the intact bone

The finite element model of the intact bone was used to validate the bone remodelling model, i.e., to understand to what extent the model could successfully reproduce the actual bone density distribution of

the subject under analysis. For that, different values for the parameter k, ranging from 0.1×10^{-4} to 0.5×10^{-3}, and the parameter m, ranging from 3 to 6, were evaluated to assess which combination of these parameters results in the nearest qualitative solution to the CT images. For comparison purposes, all simulations were performed for 300 iterations.

In order to start the bone remodelling simulation from a more accurate solution, the density values of bone were estimated from the CT images used to create the geometric model of humerus. Each pixel of the CT image is assigned with a numerical value, known as CT gray value. This value is the average of all the attenuation values, μ, contained within the corresponding voxel and is converted into a dimensionless scale, Hounsfield units (HU), by comparison with the attenuation value of water, μ_{water}, being expressed as (Buzug, 2008):

$$CT\ value = 1000 \times \frac{\mu - \mu_{water}}{\mu_{water}} \tag{4-2}$$

where the CT value is given in Hounsfield units. The apparent density, ρ_{ap} can be computed from the CT values using a linear calibration. This calibration is calculated from two reference points of the CT images. The first point is the CT value of air (minimum CT value), representing the non-bone condition with $\rho_{ap} = 0\ kg\ m^{-3}$. The second point is the CT value of cortical bone (maximum CT value), with $\rho_{ap} = 1800\ kg\ m^{-3}$ (Gupta & Dan, 2004). The equation of the calibration is given by

$$\rho_{ap} = a + b \times\ CT\ value \tag{4-3}$$

where a and b are constant parameters obtained through the calibration.

Using bonemapy (version 0.4.1, 2013), a freeware plug-in for Abaqus (Hogg, 2013), the CT values of the humerus were obtained through the overlapping of the stack of CT images, used in the acquisition of the geometric model of humerus, and the finite element mesh of the humerus. The bonemapy returns the CT value of each FE mesh node. A routine in Matlab® was implemented to calculate the relative density distribution in bone for each mesh node, through the calibration in equation 4-3. It is worth mentioning that the apparent density of bone, ρ_{ap} is related to the relative density, ρ by the expression $\rho_{ap}(kg\ m^{-3}) = 1800\ \rho$, to the extent that $1800\ kg\ m^{-3}$ is considered the maximum bone apparent density of cortical bone.

The initial relative density distribution of bone, i.e., the one inferred from the CT images before the process of bone remodelling, presented higher density in the superficial nodes (cortical bone) and lower in the inner nodes (trabecular bone), as expected. However, since each pixel in a CT image characterizes the attenuation properties of a specific material volume, when the signal-generating components are not uniform within a voxel, the CT value denotes an average of the pixels' properties, which may not correspond to reality (Ketcham & Carlson, 2001; Tang et al., 1993). This occurrence is known as partial-volume effect and appears in all material boundaries, which leads to inaccuracies in the definition of its density values.

Therefore, the maximum relative density listed among all nodes was assigned to the superficial nodes in order to correct the partial volume effect and define the expected outer shell of cortical bone.

During the bone remodelling simulation, the relative density at all nodes could range from a minimum of 0.0012 and a maximum of 0.972.

4.3.2 Bone remodelling of the humerus after the shoulder arthroplasty

The bone remodelling simulations were performed considering a healthy condition and a poor bone quality condition. For a healthy condition, the bone remodelling analyses for each model of the implanted bone were performed using the k and m parameters selected in the validation of the bone remodelling model with the intact bone. A poor bone quality condition of bone was also assessed by considering a higher cost of bone maintenance. Based on the results reported by Santos et al. (2010), the parameter k was defined 4.7 times larger than that of the healthy condition. The simulations were performed for 300 iterations.

The initial bone material properties were defined using the final density distribution of the bone remodelling simulation of the intact humerus, for each condition of bone. That way, the simulation starts from a more realistic condition. Given that the meshes of the implanted and intact models are different, a Matlab® routine was developed to map the densities from the nodes of the intact model to the nodes of the implanted model. This was achieved by calculating a weighted average of densities based on the distance of the nearest nodes of the intact bone with respect to the nodes of the implanted bone.

4.4 Evaluation of the results

4.4.1 Validation of the bone remodelling model for intact bone

The resulting bone density distributions were evaluated, qualitatively, by visual comparison with the CT images and, quantitatively, by comparing the bone relative density values from the bone remodelling analyses with the real relative density values from the CT images, based on a statistical analysis (Quental, Folgado, et al., 2014). The root-mean-square (RMS) error between these was calculated based on an absolute and relative difference, $\Delta\rho_a$ and $\Delta\rho_r$, respectively, expressed as:

$$\Delta\rho_a = \left|\rho_i^{REM} - \rho_i^{CT}\right| \tag{4-4}$$

$$\Delta\rho_r = \left|\frac{\rho_i^{REM} - \rho_i^{CT}}{\rho_i^{CT}}\right| \tag{4-5}$$

where, ρ_i^{REM} and ρ_i^{CT} represent the bone relative densities of node i resulting from the bone remodelling analyses and the CT images, respectively. The mean and standard deviation (SD) of bone density distribution were also computed, for each bone remodelling analysis.

Due to the design of the implants modelled, the humeral head is the most important region. Therefore, the RMS error, mean and SD were computed only for the humeral head up to the surgical neck.

4.4.2 Bone remodelling of the humerus after the shoulder arthroplasty

In order to evaluate how bone adapts in the presence of an implant, qualitative and quantitative comparisons were evaluated. For the qualitative analysis, the absolute difference in bone relative density was assessed between the final and the initial solutions of the bone remodelling analyses for the implanted bone.

For the quantitative analysis, the proximal region of the humerus was divided into twelve and eight regions of interest, ROI, for the implanted bone with Global CAP and Sidus, respectively, as depicted in Figure 4-17 and Figure 4-18 (Schmidutz et al., 2014). The number of regions is different for the two implanted bones because of their difference in design. Nonetheless, the first eight regions are comparable for both implants. The bone was first divided in half to select the region of the humeral head. This was achieved by passing a plane parallel to the proximal end of the bone, a few millimetres away from the last node of the humerus in contact with the implants. Then, the head was longitudinally divided into anterior-posterior and medial-lateral sections using the cruciform shape of both anchor and stem of the Sidus and Global CAP implants, respectively. For the Global CAP implanted bone other two transversal planes were defined: one passing through the base of the implant's head and another one in the middle, equidistant from the previously described plane and the one that selects the whole region of the humeral head. Finally, for the Sidus implanted bone only the middle transversal plane described before was defined. It is worth mentioning that, although the cutting planes of the humeral head for the two implants have the same orientation, they are distanced by an offset of 2.5mm, as it can be perceived by Figure 4-19.

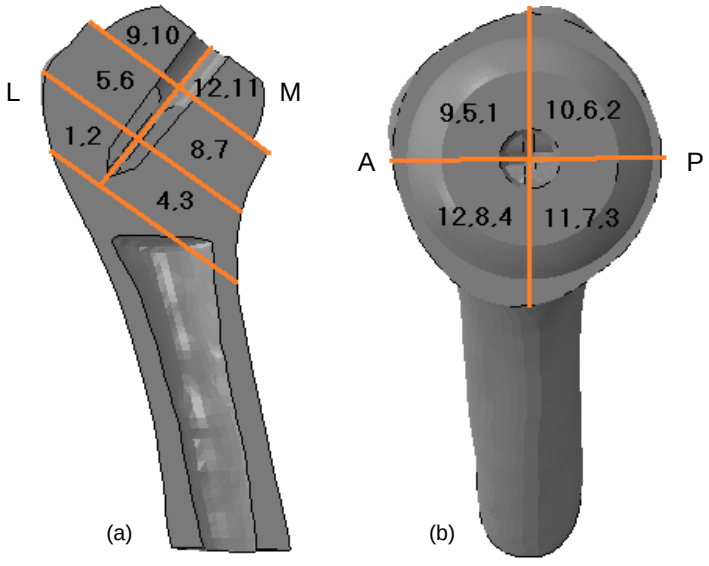

Figure 4-17 Regions of interest for the analyses of the bone remodelling simulations of the implanted humerus with Global CAP: (a) anterior view, and (b) medial view.

The change in bone mass, calculated for each ROI, is given by

$$\Delta m(\%) = \frac{\sum_{i=1}^{n}(\rho_i^{final} - \rho_i^{initial}) \times \mathrm{V}_i}{\sum_{i=1}^{n} \rho_i^{initial} \times \mathrm{V}_i} \times 100 \quad (4\text{-}6)$$

where n is the total number of nodes within the ROI under analysis, ρ_i^{final} and $\rho_i^{initial}$ are the bone relative densities of node i ($i \in ROI$) at the end and beginning of the bone remodelling simulation, respectively, and V_i is the volume associated to the node i (Quental, Fernandes, et al., 2014). The computation of the change in bone mass for each ROI allows a better perception of the local behaviour of bone in relation to its formation and resorption.

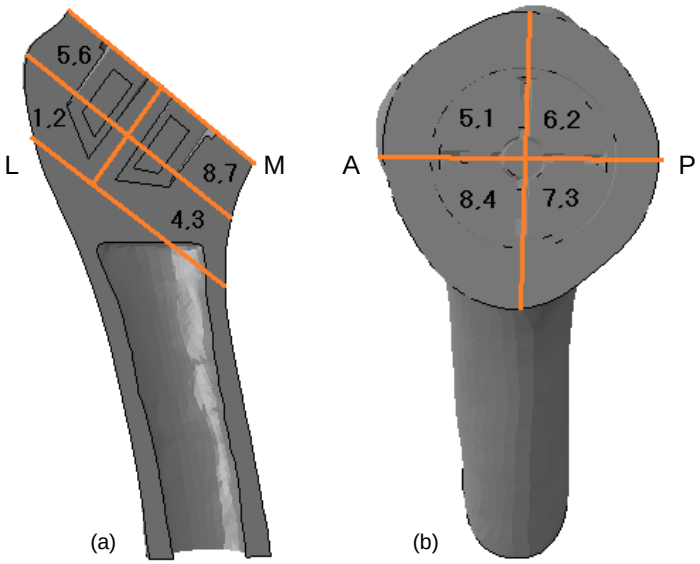

Figure 4-18 Regions of interest for the analyses of the bone remodelling simulations of the implanted humerus with Sidus: (a) anterior view, and (b) medial view.

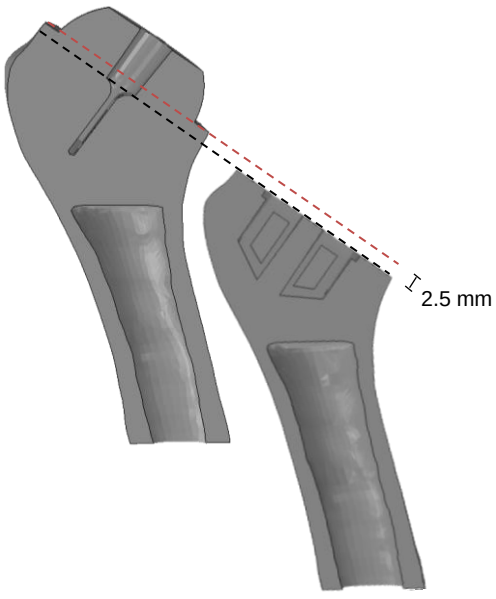

Figure 4-19 Cutting planes defined to position the humeral head implant for both prostheses, separated by an offset of 2.5 mm (anterior view).

Chapter 5

Results

This chapter presents the results of the bone remodelling analyses. At first, the results of the validation of the bone remodelling model are described. Then, the bone density distribution is evaluated qualitatively and quantitatively for the implanted bone with two implants, for both healthy and poor bone quality conditions.

5.1 Validation of the bone remodelling model for intact bone

The RMS errors of the absolute and relative differences ($\Delta\rho_a$ and $\Delta\rho_r$, respectively) between the relative density of the bone remodelling analyses and the CT images are presented in Table 5-1, along with the mean and SD. To simplify the analysis, the RMS error for both $\Delta\rho_a$ and $\Delta\rho_r$ are described graphically in Figure 5-1. For all simulations, the 300 iterations led to a solution that was changing less than 0.008% in volume, between consecutive iterations.

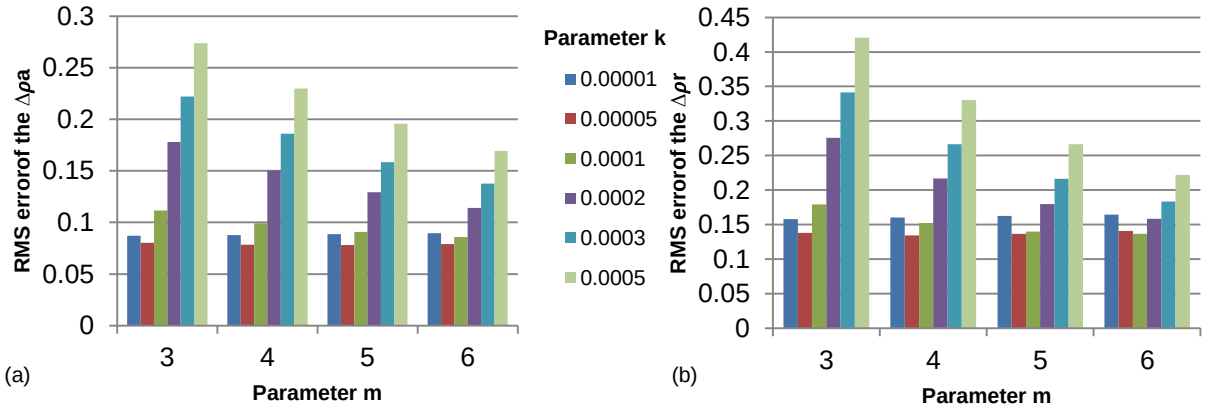

Figure 5-1 RMS error based on an absolute difference $\Delta\rho_a$ (a) and a relative difference $\Delta\rho_r$ (b) between the bone relative density of the bone remodelling analyses and the CT images.

The best solutions, i.e., the solutions with the lowest RMS errors, are characterized by the parameter k of 5×10^{-5} and the parameter m of 4 and 5, for the absolute and relative differences, respectively. It should be noted, nonetheless, that other solutions present comparable errors, and thus would also be suitable options. The mean and standard deviation (SD) of the CT images' relative densities are 0.5946 and

0.1731, respectively. Considering these measures for the bone remodelling solutions, presented in Table 5-1, it can be observed that the optimal mean density value stands for the parameters k and m of 5×10^{-5} and 4, respectively, with a mean value of 0.5977 and SD of 0.1684. Thereby, this solution is deemed as the most suitable to reproduce the bone density distribution of the analysed humerus.

Table 5-1 RMS error of $\Delta\rho_a$ and $\Delta\rho_r$ between the bone relative density of the bone remodelling analyses and the CT images; and mean and standard deviation of the performed bone remodelling analyses.

m	k	RMS error		Mean (SD)
		$(\Delta\rho_a)$	$(\Delta\rho_r)$	
3	1×10^{-5}	0.0870	0.1579	0.6421 (0.1816)
	5×10^{-5}	0.0802	0.1378	0.5864 (0.1775)
	1×10^{-4}	0.1117	0.1794	0.5299 (0.1681)
	2×10^{-4}	0.1779	0.2754	0.4550 (0.1504)
	3×10^{-4}	0.2220	0.3415	0.4095 (0.1396)
	5×10^{-4}	0.2737	0.4204	0.3565 (0.1265)
4	1×10^{-5}	0.0878	0.1601	0.6446 (0.1791)
	5×10^{-5}	0.0782	0.1344	0.5977 (0.1684)
	1×10^{-4}	0.0991	0.1522	0.5515 (0.1533)
	2×10^{-4}	0.1503	0.2169	0.4903 (0.1320)
	3×10^{-4}	0.1861	0.2662	0.4530 (0.1195)
	5×10^{-4}	0.2299	0.3302	0.4080 (0.1064)
5	1×10^{-5}	0.0888	0.1624	0.6469 (0.1775)
	5×10^{-5}	0.0781	0.1365	0.6080 (0.1629)
	1×10^{-4}	0.0907	0.1397	0.5703 (0.1457)
	2×10^{-4}	0.1293	0.1796	0.5201 (0.1231)
	3×10^{-4}	0.1586	0.2160	0.4885 (0.1106)
	5×10^{-4}	0.1957	0.2663	0.4499 (0.0971)
6	1×10^{-5}	0.0897	0.1644	0.6488 (0.1767)
	5×10^{-5}	0.0789	0.1408	0.6168 (0.1601)
	1×10^{-4}	0.0858	0.1366	0.5857 (0.1421)
	2×10^{-4}	0.1141	0.1582	0.5446 (0.1195)
	3×10^{-4}	0.1376	0.1834	0.5179 (0.1069)
	5×10^{-4}	0.1692	0.2220	0.4842 (0.0934)

The qualitative comparison between the bone remodelling solution deemed as the best and the CT images is presented in Figure 5-2. For the sake of briefness, only three horizontal slices are shown. Although differences exist between the images, the results are in general consistent and represent a reasonable approximation of the actual bone density.

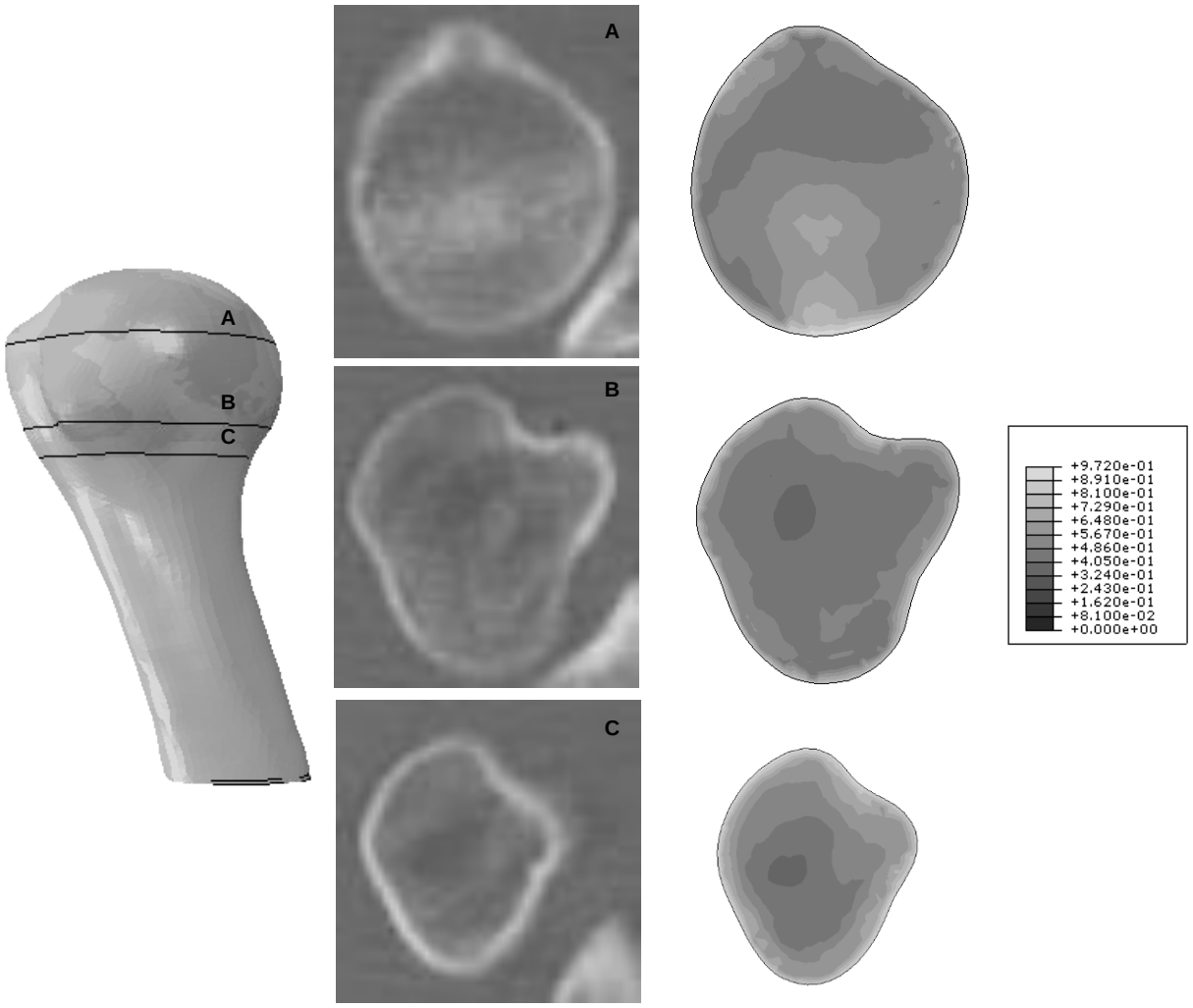

Figure 5-2 Comparison between the CT images, on the left, and the bone remodelling result, on the right, for the parameters k and m of 5×10^{-5} and 4, respectively.

5.2 Bone remodelling of the humerus after the shoulder arthroplasty

The absolute changes in the bone relative density, with respect to the initial condition of the bone remodelling analyses, are illustrated in Figure 5-3, for the implanted bone with the Global CAP and the Sidus considering healthy and poor bone quality conditions. For all simulations, the 300 iterations led to a solution that was changing less than 0.02% in volume, between consecutive iterations. The process of bone adaptation is categorized into bone apposition, equilibrium, and bone resorption. The equilibrium condition was considered for absolute variations in bone density smaller than 0.04.

No significant differences were found in the bone density distribution between the results of the Global CAP for the two type of interactions defined – without contact and with a coefficient of friction of 0.26 – between the bone and the outer rim of the Global CAP, which are illustrated in Figure 4-13. Consequently, only the results for the contact model are presented here.

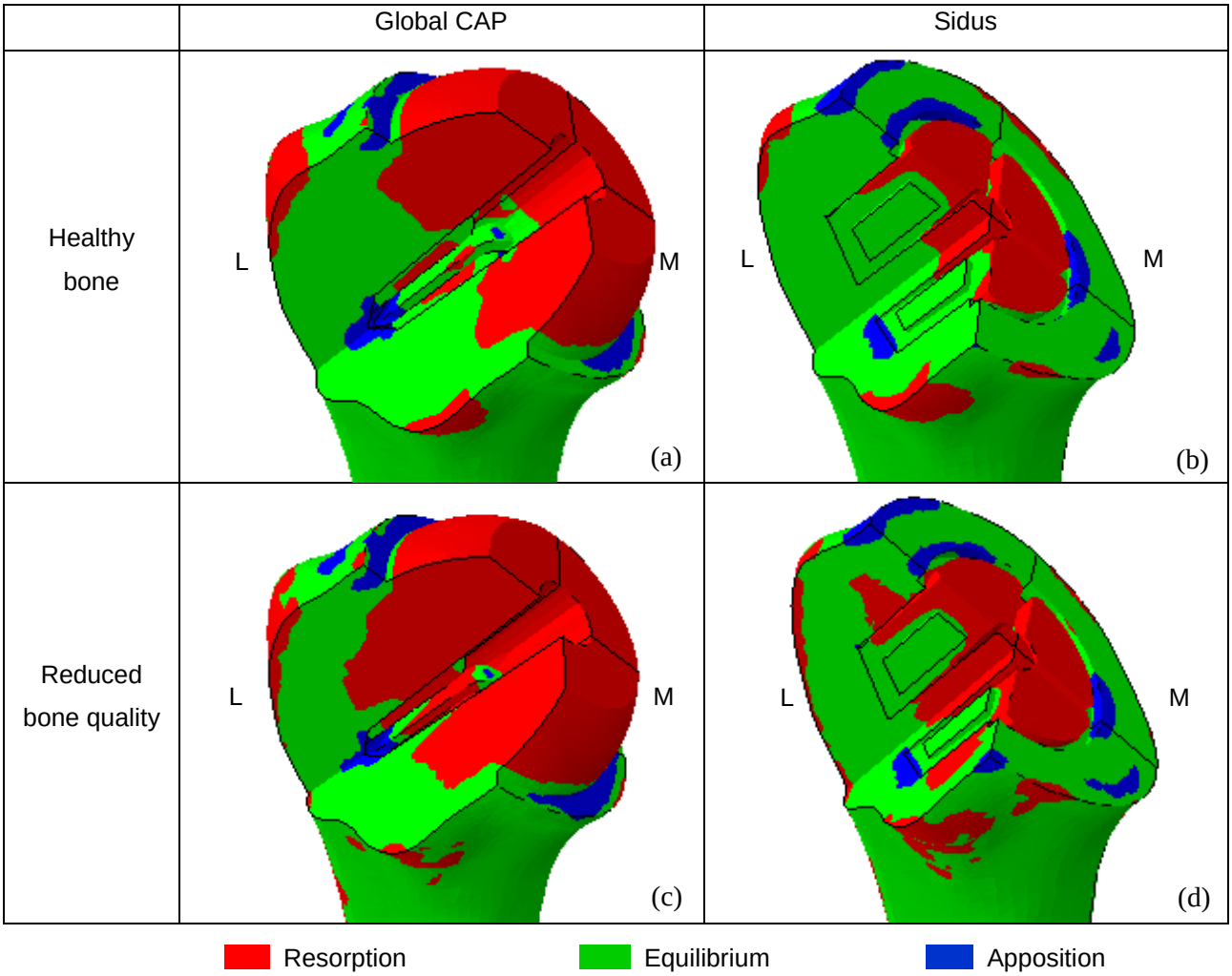

Figure 5-3 Absolute changes in bone relative density, with respect to the initial condition of the bone remodelling analyses of the implanted bone with Global CAP and Sidus, considering healthy and poor bone quality conditions (anterior view).

The changes in bone mass for the regions of interest of the implanted bone with the Global CAP and Sidus, described in detail in Figures 4-17 and 4-18, are presented in Table 5-2, for both healthy and reduced quality bones. Note that, for each ROI, values above zero indicate an increase in the bone mass whereas values below zero indicate a decrease. The global percentages of the regions 1 to 4, 5 to 8, and 9 to 12 represent the change in bone mass for the set of ROI. The ROI total-8 and total-12, in Table 5-2, represent the change in bone mass for all the 8 and 12 regions under analysis. Figures 5-4 and 5-5 present a graphical analysis of the results shown in Table 5-2.

Considering the healthy condition, the Global CAP implanted bone shows a high level of bone resorption in the proximal humerus, as illustrated in Figure 5-3 (a), indicating unloaded bone stock due to the presence of the implant. Bone apposition is mainly seen below the outer rim and below the tip of the stem of the implant. This suggests that, after the prosthesis implantation, the load is transferred predominantly

through that region. The Sidus implanted bone, depicted in Figure 5-3 (b), shows some bone resorption in the central region, where the anchor is placed. Bone apposition occurs mainly at the interface between the bone and the head of the implant, around the medial and inferior segments of the anchor and at the end of the anchorage open-fins, on the anterior and posterior sections. Quantitatively, the results are quite similar for the common regions of the two implanted humerus in the healthy condition, as it can be seen in Table 5-2. A global decrease in bone mass of 0.3% and 0.8% is seen in regions 1 to 4, for the Global CAP and Sidus implanted bones, respectively. With respect to regions 5 to 8, both implants lead to similar decreases in bone mass, of 3.8%. Nonetheless, the highest decreases in bone mass occur in regions 9 to 12 of the Global CAP implanted bone, with a global reduction of 12.8%.

Table 5-2 Changes in bone mass, in percentage, with respect to the initial condition of the bone remodelling analyses for the ROI of the implanted bone with the Global CAP and Sidus, for both healthy and reduced quality bones. Darker shaded cells denote a higher decrease of bone mass.

ROI	Healthy bone				Reduced bone quality			
	Global CAP		Sidus		Global CAP		Sidus	
1	-1.95	-0.30	-2.81	-0.76	-5.33	-3.31	-6.60	-3.91
2	0.44		0.03		-3.25		-3.63	
3	-0.11		-1.05		-2.31		-3.80	
4	0.01		0.26		-2.98		-2.49	
5	-6.35	-3.79	-6.41	-3.77	-11.22	-8.03	-10.58	-8.02
6	-2.78		-4.35		-7.61		-8.46	
7	-4.31		-2.75		-7.79		-7.43	
8	-1.69		-1.47		-5.40		-5.51	
9	-12.85	-12.84			-25.42	-25.99		
10	-13.69				-28.11			
11	-12.81				-24.94			
12	-12.02				-25.49			
Total-8	-2.23		-2.29		-5.93		-5.99	
Total-12	-4.46				-10.13			

The results obtained for a poorer condition of bone are qualitatively similar to those obtained for a healthy condition. However, the level of bone resorption increased compared to that of the healthy condition, as depicted in Figure 5-3. As expected, considering the quantitative analysis, the results are worse for the bone with reduced quality in comparison to the normal condition, for each implanted bone, as shown in Table 5-2.

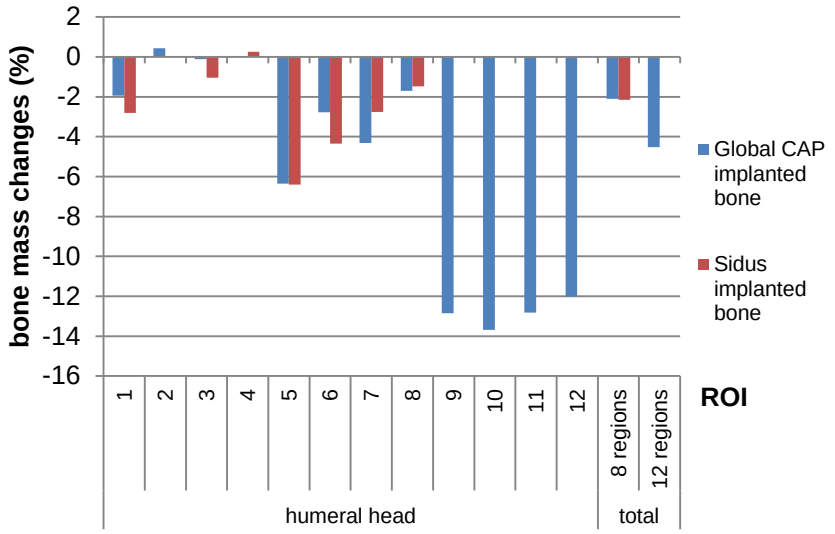

Figure 5-4 Comparison of the bone mass change, in percentage, between the implanted bone with Global CAP and Sidus, in the healthy condition, for the ROI 1 to 12 and the ROI total 8 and total 12.

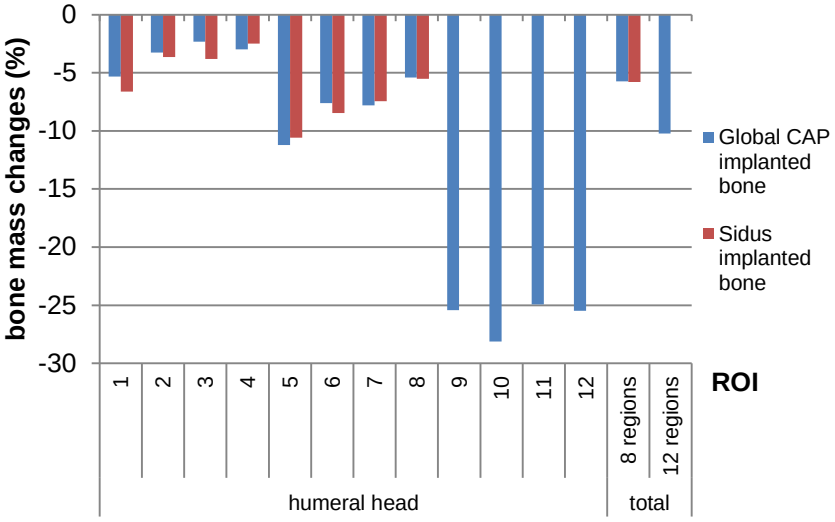

Figure 5-5 Comparison of the bone mass change, in percentage, between the implanted bone with Global CAP and Sidus, in the poor bone quality condition, for the ROI 1 to 12 and the ROI total 8 and total 12.

Chapter 6

Discussion

Recently, new implant designs have been developed to improve the long-term outcomes of shoulder arthroplasty and to provide an improved bone quality in revision operations. In the literature, there is still insufficient information regarding the effect of stress shielding in the humerus when resurfacing and stemless implants are implanted. Moreover, the bone remodelling process with respect to resurfacing and stemless shoulder arthroplasties has not been addressed in previous studies. Therefore, three-dimensional finite element models of the humerus were developed in this study, to analyse the bone remodelling process after the virtual implantation of a resurfacing implant and a stemless implant. The influence of the initial bone quality was also evaluated.

This work focused on the comparison of the bone density distribution obtained for the humerus without an implant to that obtained for the implanted humerus. The qualitative results obtained show similar levels of bone resorption for the resurfacing and stemless implants around the stem and central region of the anchor, respectively. In particular, for the Global CAP implant, decreased bone density is observed in the region underlying the resurfaced head, indicating unloaded bone stock due to the presence of the implant. On the other hand, bone apposition is observed around the outer rim of the implants and below the tip of the stem and anchorage fins, for the resurfacing and stemless implants, respectively. Quantitatively, the results are in accordance with the qualitative results, confirming a higher decrease in bone mass at the proximal region of the humerus. This reduction in the proximal bone mass is greater for the Global CAP implant, since the head is not resected and the loads are transferred through the outer shell of the implant, leading to unloaded bone stock below the implant's cap. Bone resorption decreased from the proximal to the distal part of the humeral head.

The surgical technique recommends implanting these types of prostheses only in the presence of bone with good quality (DePuy, 2004; Zimmer, 2012). The results obtained for the poor bone quality condition show an increased loss of bone at the fixation site, which might compromise the stability of the implant. In other words, the results support the recommendations of manufacturers given the limited performance of these implants for poor bone quality conditions.

Although the results confirm the incidence of stress shielding after the implantation of both prostheses, the stemless implant lost less density at the implant fixation, suggesting that, when seeking for a better support of the implant with satisfactory bone quality, stemless implants may lead to superior long-term outcomes when compared with the resurfacing implants.

The results obtained in this work for the resurfacing implant are consistent with a previous study conducted by Schmidutz et al. (2014) which evaluated stress shielding using FE analysis and bone remodelling pattern of two different shoulder resurfacing implant designs retrieved in vivo. The implant designs evaluated on that study have two different fixation methods: a central stem and a conical crown shaped ring. The results show similar pattern of stress shielding in the FE and retrieval analyses. The stress shielding is induced by an inhomogeneous pattern of strain distribution after implantation; however, for the conical crown shaped ring the results appeared more homogenous, presenting a more balanced strain pattern around the stem. The authors suggest that the use of stems that transfer the load not only to the center of bone, but also to the adjoining area might reduce the amount of unloaded bone, which is in accordance with the results obtained in the present study for the stemless implant. Also, for the models with reduced bone quality, the effect of stress shielding was in general 2-3 times higher compared to the model with a normal bone quality, which is in line with the current study. In other study, Razfar et al. (2015) investigated the effect of the implant stem length on the proximal bone stresses. Although reductions in stem length resulted in cortical bone stresses that better mimicked the proximal intact cortical bone, significantly increased stresses in proximal trabecular bone were identified for the stemless model. This happens because all the joint reaction force is transferred across the metaphyseal region where the implant is secured. Nonetheless, they considered the stemless design as the better option to mimic the intact bone after the joint replacement, although with concern about its stability.

Adequate primary stability of the implant is fundamental to guarantee the long-term success of uncemented stemless shoulder implants (Favre & Henderson, 2016). Although recent short-term follow-up studies of stemless implants have shown promising results (Churchill, 2014; Churchill & Athwal, 2016), there are no long-term studies addressing the potential outcome of stemless implants. Given that implant's design affects the local bone adaptation process, the results of a single implant should not be generalized to others. As far as the authors know, there are no clinical data available regarding the stemless implant considered in this study, neither computation models evaluating the stress shielding effect in the humerus after the shoulder arthroplasty.

Computational models addressing the effects of stress shielding have largely been applied to the hip resurfacing arthroplasty and the results seem to agree with the current work (Behrens et al., 2009; Gupta et al., 2006; Ong et al., 2006; Pal & Gupta, 2011). In the remodelling process of a cemented hip resurfacing arthroplasty, Gupta et al. (2006) described bone density reductions between 60% and 90% in the region below the resurfaced head, indicating significant bone resorption, whereas bone apposition was described around the distal tip of the implant. Also, from the proximal to the distal end of the implant, bone

resorption was reduced to a maximum of 10%. Although the majority of hip resurfacing studies focus on cement fixation, some biomechanical studies have evaluated the uncemented type of fixation (Ong et al., 2006; Pal & Gupta, 2011). Ong et al. (2006) found no differences in bone remodelling between cemented and cementless hip resurfacing implants, under comparable interface conditions. Moreover, their work found increased stress around the stem which induced bone formation, while reduced stress was described underneath the resurfacing head which led to bone resorption. Pal & Gupta (2011) reported bone density reductions and increases around 50-80% in the region underlying the resurfaced head and around the distal tip of the stem, respectively, for cementless hip resurfacing implants. Although the results described are consistent with those obtained in this work, these must be evaluated with caution since the mechanical environment and the forces acting on the hip and shoulder joints are different.

The present study overcomes some limitations of the work of Schmidutz et al. (2014). In particular, the bone adaptation process was effectively modelled to understand the effect of the resurfacing and stemless prostheses on the humerus. Six load conditions, including the action of muscle forces were considered to better characterize the mechanical environment of the bone. Additionally, this study is strengthened by the evaluation of the bone remodelling process after a stemless shoulder arthroplasty, which was never considered before by means of computational simulation.

Regardless of its contribution, this work is not without limitations. First of all, the bone geometry and density distribution were based on CT-scan data of a single representative humerus, so further studies on a subject-specific basis would be valuable. The definition of the muscle sites was based on the Atlas of Human Anatomy (Netter, 2006), aided by personal perception, and therefore susceptible to inaccuracies. The present study was strengthened by the use of 6 load cases but the application of more load cases may improve the bone remodelling simulations. The osteointegration process was not modelled. Idealized conditions of complete osteointegration were considered. Since it was not possible to obtain the physical models of the implants, these were modelled according to the surgical techniques (DePuy, 2004; Zimmer, 2012). Thus, some variations with respect to the original design may exist. The significant differences in the design of each implant made the comparison between them difficult to perform. For instance, although the approach to define the regions of interest was the same in both cases – i.e., the regions were defined using the cruciform shape of the stem and anchor, for the resurfacing and stemless implants, respectively –, the defined regions of interest (1 to 8) present slight variations between the two models.

In conclusion, even though there is still lack of knowledge in the literature regarding the outcomes of both resurfacing and stemless shoulder arthroplasties, the results of this study are coherent with previous studies and are expected to provide some clarification about the influence of different shoulder implants on the bone remodelling process of the humerus. Similar levels of bone resorption were observed for the resurfacing and stemless implants. However, the stemless implant lost less density at the implant fixation, which suggests that the stemless implants may be better supported in the long-term, and thus can lead to a better outcome than the resurfacing implants.

Chapter 7

Conclusion

Numerical simulations are valuable tools to predict how bones adapt to different loads after the implantation of a prosthesis, without the need to rely on subjects' dependent clinical trials. In the present work, computational models were developed to study the influence of resurfacing and stemless implants on the process of bone adaptation of the humerus.

The results revealed that the implanted bones were affected by the phenomenon of stress shielding. In particular, a comparison between the intact model and the implanted models revealed similar levels of bone resorption for the resurfacing and stemless implants around the stem and anchor fixation sites, respectively. In addition, for the resurfacing implant, high bone resorption was verified at the region underneath the head cap, indicating unloaded bone stock. Bone apposition was observed around the outer rim of the implants and below the tip of the stem and anchorage fins for the resurfacing and stemless implants, respectively. Nonetheless, the loss of bone density was smaller at the implant fixation of the stemless model, which suggests that stemless implants may be better supported in the long-term than resurfacing implants. For the poor bone quality condition, the loss of bone increased, which supports the limited performance of these implants for reduced bone stock.

Although this study presents a relevant contribution to a better understanding of the process of bone remodelling of the humerus after resurfacing and stemless arthroplasties, future studies should address some of its limitations. For instance, to confirm the results obtained for a single humerus, future works should consider a larger number of humeri. Considering that little is known in the literature about the long-term outcomes of stemless shoulder arthroplasty, it would be interesting to compare the bone adaptation process for different stemless implants, given the distinctive differences that exist in design. Additionally, other critical factors, such as stability, also need to be studied. Subsequent studies may evaluate the stability of the implant after the bone remodelling process in order to understand what are the consequences of the loss of bone density in the long-term support of the implant.

References

Behrens, B., Nolte, I., Wefstaedt, P., Stukenborg-colsman, C., Bouguecha, A., & Modeling, A. (2009). Finite Element Analysis of Bone Remodeling after Hip Resurfacing Arthroplasty *1*(1):2288–2291.

Bohsali, K. I., Bois, A. J., & Wirth, M. A. (2017). Complications of Shoulder Arthroplasty. The Journal of Bone and Joint Surgery-American Volume *99*(3):256–269.

Boileau, P., Sinnerton, R. J., Chuinard, C., & Walch, G. (2006). Arthroplasty of the shoulder. Journal of Bone and Joint Surgery - British Volume *88–B*(5):562–575.

Burgess, D. L., McGrath, M. S., Bonutti, P. M., Marker, D. R., Delanois, R. E., & Mont, M. A. (2009). Shoulder Resurfacing. The Journal of Bone and Joint Surgery-American Volume *91*(5):1228–1238.

Buzug, T. M. (2008). Computed tomography: from photon statistics to modern cone-beam CT. Springer Science & Business Media.

Chan, A. (2014). Biomechanical analysis of the influence of different tibial tray designs in TKA. Instituto Superior Técnico.

Churchill, R. S. (2014). Stemless shoulder arthroplasty: Current status. Journal of Shoulder and Elbow Surgery *23*(9):1409–1414.

Churchill, R. S., & Athwal, G. S. (2016). Stemless shoulder arthroplasty—current results and designs. Current Reviews in Musculoskeletal Medicine *9*(1):10–16.

Cignoni, P., Callieri, M., Corsini, M., Dellepiane, M., Ganovelli, F., & Ranzuglia, G. (2008). MeshLab: an Open-Source Mesh Processing Tool. Sixth Eurographics Italian Chapter Conference 129–136.

Clarke, B. (2008). Normal bone anatomy and physiology. Clinical Journal of the American Society of Nephrology : CJASN *3 (Suppl 3*:131–139.

Coley, B., Jolles, B. M., Farron, A., & Aminian, K. (2008). Arm position during daily activity. Gait and Posture *28*(4):581–587.

Coley, B., Jolles, B. M., Farron, A., & Aminian, K. (2009). Detection of the movement of the humerus during daily activity. Medical and Biological Engineering and Computing *47*(5):467–474.

Culham, E., & Peat, M. (1993). Functional Anatomy of the Shoulder Complex. Journal of Orthopaedic and Sports Physical Therapy *18*(1):342–350.

Dassault. (2012). ABAQUS User's Manual. ABAQUS/CAE User's Manual.

DePuy. (2004). Surgical technique - Resurfacing Humeral Head Implant. England: DePuy International Ltd.

Eberle, S., & Augat, P. (2007). Preventing Contact Convergence Problems in Bone - Implant Contact Models. In *ANSYS Conference 25th CADHEM Users Meeting 2007* (pp. 21–25). Dresden.

Favre, P., & Henderson, A. (2016). Prediction of stemless humeral implant micromotion during upper limb activities. Clinical Biomechanics *36*:46–51.

Favre, P., Snedeker, J. G., & Gerber, C. (2009). Numerical modelling of the shoulder for clinical applications. Philosophical Transactions of the Royal Society A: Mathematical, Physical and Engineering Sciences *367*(1895):2095–2118.

Fernandes, P. R., Folgado, J., Jacobs, C., & Pellegrini, V. (2002). A contact model with ingrowth control for bone remodelling around cementless stems. Journal of Biomechanics *35*(2):167–176.

Fernandes, P., Rodrigues, H., & Jacobs, C. (1999). A Model of Bone Adaptation Using a Global Optimisation Criterion Based on the Trajectorial Theory of Wolff. Computer Methods in Biomechanics and Biomedical Engineering *2*(2):125–138.

Folgado, J., Fernandes, P. R., Guedes, J., & Rodrigues, H. (2004). Evaluation of osteoporotic bone quality by a computational model for bone remodeling. Computers & Structures *82*(17–19):1381–1388.

Friedman, R. J., Cj, F., Laberge, M., Dooley, R. L., & Hara, A. L. O. (1992). Finite element modeling of the glenoid component : EHect of design parameters on stress distribution. Journal of Shoulder and Elbow Surgery *1*(5):261–270.

Gartsman, G., & Edwards, T. B. (2008). Shoulder Arthroplasty (First). Elsevier.

Geraldes, D. M., Modenese, L., & Phillips, A. T. M. (2016). Consideration of multiple load cases is critical in modelling orthotropic bone adaptation in the femur. Biomechanics and Modeling in Mechanobiology *15*(5):1029–1042.

Guedes, J., & Kikuchi, N. (1990). Preprocessing and postprocessing for materials based on the homogenization method with adaptive finite element methods. Computer Methods In Applied Mechanics and Engineering *83*(2):143–198.

Gupta, S., & Dan, P. (2004). Bone geometry and mechanical properties of the human scapula using

computed tomography data. Trends Biomater Artif Organs *17*(2):61–70.

Gupta, S., New, A. M. R., & Taylor, M. (2006). Bone remodelling inside a cemented resurfaced femoral head *21*:594–602.

Gupta, S., Van der Helm, F. C. T., & Van Keulen, F. (2004). The possibilities of uncemented glenoid component — a finite element study. Clinical Biomechanics *19*(3):292–302.

Hogg, M. (2013). bonemapy 0.4.1 : Python Package Index. Retrieved October 19, 2017, from https://pypi.python.org/pypi/bonemapy/

Hopkins, A. R., Hansen, U. N., Amis, A. A., & Emery, R. (2004). The effects of glenoid component alignment variations on cement mantle stresses in total shoulder arthroplasty. Journal of Shoulder and Elbow Surgery *13*(6):668–675.

Jacobs, C., Levenston, M., Beaupré, G., Simo, J., & Carter, D. (1995). Numerical instabilities in bone remodeling simulations: The advantages of a node-based finite element approach. Journal of Biomechanics *28*(4):449–459.

Katz, D., O'Toole, G., Cogswell, L., Sauzieres, P., & Valenti, P. (2007). A history of the reverse shoulder prosthesis. International Journal of Shoulder Surgery *1*(4):108–113.

Ketcham, R. A., & Carlson, W. D. (2001). Acquisition, optimization and interpretation of x-ray computed tomographic imagery: Applications to the geosciences. Computers and Geosciences *27*(4):381–400.

Klawitter, J. J., More, R. B., Gourley, M. R., Ritz, J. P., & Podnos, E. G. (2014). Humeral head resurfacing implant. Google Patents. Retrieved from http://www.google.com.na/patents/US8690958

Knudson, D. (2007). Fundamentals of Biomechanics (Second). New York, NY: Springer US.

Lacroix, D., Murphy, L. A., & Prendergast, P. J. (2016). Three-Dimensional Finite Element Analysis of Glenoid Replacement Prostheses : A Comparison of Keeled and Pegged Anchorage Systems *122*(4):430–436.

Levangie, P. K., & Norkin, C. C. (2005). Joint Structure and Function: A Comprehensive analysis (Fourth). Philadelphia, PA: F.A. Davis Company.

Levy, O. (2016). Humeral Head Resurfacing Arthroplasty. In A. D. Armstrong & A. M. Murthi (Eds.), *Anatomic Shoulder Arthroplasty: Strategies for Clinical Management* (pp. 41–56). Cham: Springer International Publishing.

Levy, O., Pearse, E., Even, T., Raj, D., Abrahams, R., Narvani, A., & Copeland, S. (2010). S-8 Hemiarthroplasty versus Total Shoulder Arthroplasty with the Surface Replacement Arthroplasty:

Functional Outcome and Survival Analysis. In *11th International conference on Shoulder and Elbow Surgery ICSES 2010*. Edinburgh.

Little, N., Rogers, B., & Mark, F. (2011). Bone formation, remodelling and healing. Surgery *29*(4):141–145.

Marshall, W. J., Lapsley, M., Day, A. P., & Ayling, R. M. (2014). Clinical Biochemistry: Metabolic and Clinical Aspects (Third). Churchil Livingstone Elsevier.

Nagels, J., Stokdijk, M., & Rozing, P. M. (2003). Stress shielding and bone resorption in shoulder arthroplasty. Journal of Shoulder and Elbow Surgery *12*(1):35–39.

Netter, F. H. (2006). Atlas of Human Anatomy (Fourth). Saunders/Elsevier.

Nordin, M., & Frankel, V. H. (2001). Basic Biomechanics of the Musculoskeletal System (Third). Philadelphia, PA: Lippincott Williams & Wilkins.

Ong, K. L., Kurtz, S. M., Manley, M. T., Rushton, N., Mohammed, N. A., & Field, R. E. (2006). Biomechanics of the Birmingham hip resurfacing arthroplasty. The Journal of Bone and Joint Surgery. British Volume *88–B*(8):1110–1115.

Pal, B., & Gupta, S. (2011). The effect of primary stability on load transfer and bone remodelling within the uncemented resurfaced femur. Proceedings of the Institution of Mechanical Engineers. Part H, Journal of Engineering in Medicine *225*(6):549–561.

Palastanga, N., & Soames, R. (2012). Anatomy and Human Movement: Structure and function (Sixth). Churchil Livingstone Elsevier.

Petriccioli, D., Bertone, C., & Marchi, G. (2015). Stemless shoulder arthroplasty: a literature review. Joints *3*(1):38–41.

Pham, D. L., Xu, C., & Prince, J. L. (2000). Current methods in medical image segmentation. Annu. Rev. Biomed. Eng. *2*:315–337.

Poelert, S., Valstar, E., Weinans, H., & Zadpoor, A. A. (2013). Patient-specific finite element modeling of bones. Proceedings of the Institution of Mechanical Engineers, Part H: Journal of Engineering in Medicine *227*(4):464–478.

Quental, C. (2013). Biomechanical tools for the analysis of the native and prosthetic shoulders. Instituto Superior Técnico.

Quental, C., Fernandes, P. R., Monteiro, J., & Folgado, J. (2014). Bone remodelling of the scapula after a total shoulder arthroplasty. Biomechanics and Modeling in Mechanobiology *13*(4):827–838.

Quental, C., Folgado, J., Fernandes, P. R., & Monteiro, J. (2012). Bone remodelling analysis of the humerus after a shoulder arthroplasty. Medical Engineering and Physics *34*(8):1132–1138.

Quental, C., Folgado, J., Fernandes, P. R., & Monteiro, J. (2014). Subject-specific bone remodelling of the scapula. Computer Methods in Biomechanics and Biomedical Engineering *17*(10):1129–1143.

Quilez, M. P., Seral, B., & Pérez, M. A. (2017). Biomechanical evaluation of tibial bone adaptation after revision total knee arthroplasty: A comparison of different implant systems. PLOS ONE *12*(9):1–14.

Rachner, T. D., Khosla, S., & Hofbauer, L. C. (2011). Osteoporosis: Now and the future. The Lancet *377*(9773):1276–1287.

Razfar, N., Reeves, J. M., Langohr, D. G., Willing, R., Athwal, G. S., & Johnson, J. A. (2015). Comparison of proximal humeral bone stresses between stemless, short stem , and standard stem length: a finite element analysis. Journal of Shoulder and Elbow Surgery *25*(7):1076–1083.

Reddy, J. N. (2006). An Introduction to the Finite Element Method (Third). New York, NY: McGraw-Hill.

Ribeiro, N. S., Fernandes, P. C., Lopes, D. S., Folgado, J., & Fernandes, P. R. (2009). 3-D solid and finite element modeling of biomechanical structures - A software pipeline. In *7th EUROMECH Solid Mechanics Conference*. Lisbon.

Rothstock, S., Uhlenbrock, A., Bishop, N., Laird, L., Nassutt, R., & Morlock, M. (2011). Influence of interface condition and implant design on bone remodelling and failure risk for the resurfaced femoral head. Journal of Biomechanics *44*(9):1646–1653.

Ruben, R. B., Fernandes, P. R., & Folgado, J. (2012). On the optimal shape of hip implants. Journal of Biomechanics *45*(2):239–246.

Saladin, K. S., Gan, C. A., & Cushman, H. N. (2018). Anatomy & physiology : the unity of form and function (Eighth). New York, NY: McGraw-Hill Education.

Sanchez-Sotelo, J. (2009). Reverse total shoulder arthroplasty. Clinical Anatomy *22*(2):172–182.

Sanchez-Sotelo, J. (2011). Total Shoulder Arthroplasty. The Open Orthopaedics Journal *5*:106–114.

Santos, L., Romeu, J. C., Canhão, H., Fonseca, J. E., & Fernandes, P. R. (2010). A quantitative comparison of a bone remodeling model with dual-energy X-ray absorptiometry and analysis of the inter-individual biological variability of femoral neck T-score. Journal of Biomechanics *43*(16):3150–3155.

Schmidutz, F., Agarwal, Y., Müller, P. E., Gueorguiev, B., Richards, R. G., & Sprecher, C. M. (2014). Stress-shielding induced bone remodeling in cementless shoulder resurfacing arthroplasty: A finite

element analysis and in vivo results. Journal of Biomechanics *47*(14):3509–3516.

Sharma, G. B., Debski, R. E., McMahon, P. J., & Robertson, D. D. (2010). Effect of glenoid prosthesis design on glenoid bone remodeling: Adaptive finite element based simulation. Journal of Biomechanics *43*(9):1653–1659.

Sharma, G. B., & Robertson, D. D. (2013). Adaptive scapula bone remodeling computational simulation: Relevance to regenerative medicine. Journal of Computational Physics *244*:312–320.

Sheridan, B. D., Ahearn, N., Tasker, A., Wakeley, C., & Sarangi, P. (2012). Shoulder arthroplasty. Part 1: Prosthesis terminology and classification. Clinical Radiology *67*(7):709–715.

Singh, V. (2014). Textbook of Anatomy: Upper Limb and Thorax, Volume I (Second). Reed Elsevier India Private Limited.

Sobocinski, M. (2015). Analysis of biobearings friction and wear processes. Journal of Applied Mathematics and Computational Mechanics *14*(2):103–109.

Somerson, J. S., Bois, A. J., & Wirth, M. A. (2016). Interposition Shoulder Arthroplasty. In A. D. Armstrong & A. M. Murthi (Eds.), *Anatomic Shoulder Arthroplasty: Strategies for Clinical Management* (pp. 121–127). Cham: Springer International Publishing.

Spitzer, V., Ackerman, M. J., Scherzinger, a L., & Whitlock, D. (1996). The visible human male: a technical report. Journal of the American Medical Informatics Association *3*(2):118–130.

Stone, K. D., Grabowski, J. J., An, K. N., Cofield, R. H., & Morrey, F. (1999). Stress analyses arthroplasty of glenoid components in total shoulder. Journal of Shoulder and Elbow Surgery *8*(2):151–158.

Suárez, D. R., Weinans, H., & Van Keulen, F. (2012). Bone remodelling around a cementless glenoid component. Biomechanics and Modeling in Mechanobiology *11*(6):903–913.

Tadepalli, S. C., Erdemir, A., & Cavanagh, P. R. (2011). Comparison of hexahedral and tetrahedral elements in finite element analysis of the foot and footwear. Journal of Biomechanics *44*(12):2337–2343.

Tang, C., Blatter, D. D., & Parker, D. L. (1993). Accuracy of phase-contrast flow measurements in the presence of partial-volume effects. Journal of Magnetic Resonance Imaging *3*(2):377–385.

Taylor, M., & Prendergast, P. J. (2015). Four decades of finite element analysis of orthopaedic devices: Where are we now and what are the opportunities? Journal of Biomechanics *48*(5):767–778.

Tortora, G. J., & Derrickson, B. (2010). Introduction to the human body: the essentials of anatomy and physiology (Eighth). New York, NY: John Wiley & Sons, Inc.

Total Shoulder Replacement (Arthroplasty). (n.d.). Retrieved October 26, 2017, from http://www.moveforwardpt.com/SymptomsConditionsDetail.aspx?cid=4e1deb00-f6fd-40d4-b28c-28319f0d6d4a

Wiater, J. M., & Fabing, M. H. (2009). Shoulder arthroplasty: prosthetic options and indications. The Journal of the American Academy of Orthopaedic Surgeons *17*(7):415–425.

Wilk, K. E., Reinold, M. M., & Andrews, J. R. (2009). The Athlete's Shoulder (Second). Philadelphia, PA: Churchil Livingstone Elsevier.

Yushkevich, P. A., Piven, J., Hazlett, H. C., Smith, R. G., Ho, S., Gee, J. C., & Gerig, G. (2006). User-guided 3D active contour segmentation of anatomical structures: Significantly improved efficiency and reliability. NeuroImage *31*(3):1116–1128.

Zheng, M., Zou, Z., Bartolo, P. J., Peach, C., & Ren, L. (2017). Finite element models of the human shoulder complex : a review of their clinical implications and modelling techniques. International Journal forNumerical Methods inBiomedicalEngineering *33*(2):e02777.

Zimmer. (2012). Sidus Stem-Free Shoulder - Surgical Technique. Zimmer.